Air quality and radiative impacts of downward propagating sudden stratospheric warmings (SSWs)

Ryan S. Williams[1,2], Michaela I. Hegglin[1,3], Patrick Jöckel[4], Hella Garny[4] and Keith P. Shine[1]

[1]Department of Meteorology, University of Reading, Reading, RG6 6ET, United Kingdom
5   [2]British Antarctic Survey, Cambridge, CB3 0ET, United Kingdom
[3]Institute of Energy and Climate Research, IEK-7: Stratosphere, Forschungszentrum Jülich, Jülich, 52425, Germany
[4]Deutsches Zentrum für Luft- und Raumfahrt (DLR), Institut für Physik der Atmosphäre, Oberpfaffenhofen, 82234, Germany

Correspondence to: Michaela I. Hegglin (m.i.hegglin@reading.ac.uk)

Abstract. Sudden stratospheric warmings (SSWs) are abrupt disturbances to the Northern Hemisphere wintertime
10   stratospheric polar vortex that can lead to pronounced regional changes in surface temperature and precipitation. SSWs also
strongly impact the distribution of chemical constituents within the stratosphere, but the implications of these changes for
stratosphere-troposphere exchange (STE) and radiative effects in the upper troposphere-lower stratosphere (UTLS) have not
been extensively studied. Here we show, based on a specified-dynamics simulations from the EMAC chemistry-climate model,
that SSWs lead to a pronounced increase in high-latitude ozone just above the tropopause (>25 % relative to climatology),
15   persisting for up to 50 days for the ~50 % events classified as downward propagating following Hitchcock et al. (2013). This
anomalous feature in lowermost stratospheric ozone is verified from ozone-sonde soundings and using the Copernicus
Atmospheric Monitoring Service (CAMS) atmospheric composition reanalysis product. A significant dipole anomaly (>±25
%) in water vapour also persists in this region for up to 75 days, with a drying signal above a region of moistening, also evident
within the CAMS reanalysis. An enhancement in STE leads to a significant 5−10% increase in near-surface ozone of
20   stratospheric origin over the Arctic, with a typical time-lag between 20 and 80 days. The signal also propagates to mid-latitudes
leading to significant enhancements in UTLS ozone, and, of weakening strength, also in free tropospheric and near-surface
ozone up to 90 days after the event. In quantifying the potential significance for surface air quality breaches above ozone
regulatory standards, a risk enhancement of up to a factor of 2 to 3 is calculated following such events. The chemical
composition perturbations in the Arctic UTLS result in radiatively-driven Arctic stratospheric temperature changes of around
25   2 K. An idealised sensitivity evaluation highlights the changing radiative importance of both ozone and water vapour
perturbations with seasonality. Our results highlight that whilst any background increase in near-surface ozone due to SSW-
related stratosphere-to-troposphere (STT) transport is likely to be small, this could be of greater importance locally (e.g.,
mountainous regions more susceptible to elevated ozone levels). Accurate representation of UTLS composition (namely ozone
and water vapour), through its effects on local temperatures, may also help improve numerical weather prediction forecasts on
30   sub-seasonal to seasonal timescales.

1 Introduction

Sudden stratospheric warmings (SSWs) comprise the largest deviations from the mean state in the wintertime Northern Hemisphere extratropical stratosphere (Baldwin et al., 2021), with a frequency of ~6 events per decade (Charlton et al., 2007).
35 Such events are defined by a reversal of the climatological polar temperature gradient and a change in the 60°N circumpolar mean wind from westerly to easterly at 10 hPa (~30 km) (Andrews et al., 1987). Whilst such events are commonly classified according to a dynamical distinction (e.g., vortex displacement versus split events), other demarcations have been used and may be more applicable for certain studies. For example, Nakagawa and Yamazaki (2006) used the upward propagating zonal wavenumber 2 flux to determine sub-categories of either downward or non-downward propagating SSWs. Hitchcock et al.
40 (2013) identified midwinter SSWs as either Polar-night Jet Oscillation (PJO) and non-PJO (nPJO) events. Such distinction is related to the depth to which the warming descends through the stratosphere, which is closely associated with the magnitude of upward and poleward directed wave forcing, with SSWs categorised as PJO events where the polar-cap averaged temperature anomaly is largest in the lower stratosphere (~60 hPa), provided the anomaly is sufficiently strong (de la Cámara et al., 2018b). Classification using this distinction measure has been demonstrated to illustrate the much stronger impact on
45 chemical composition of the lower stratosphere following PJO-type events, facilitated by deeper propagation down to the lowermost stratosphere (LMS) (tropopause to 100 hPa) and known dynamical persistence timescales of up to 2–3 months in this region (Hitchcock et al., 2013; de la Cámara et al., 2018a).

The increased incidence of major wintertime cold air outbreaks across the Northern Hemisphere, particularly over Eurasia (Kretschmer et al., 2018a), during either stratospheric weak vortex or SSW events has been a subject of much attention in
50 recent years (Thompson et al., 2002; Kolstad et al., 2010; Kretschmer et al., 2018b), given the potential for significant advances in sub-seasonal predictive skill (Sigmond et al., 2013; Scaife et al., 2016). Intrinsic to such changes is the equatorward displacement of the tropospheric jet stream and associated storm tracks as the stratospheric jet weakens (Baldwin and Dunkerton, 1999; Baldwin and Dunkerton, 2001; Domeisen et al. 2013; Kidston et al., 2015). SSWs are often initiated by the upward propagation of planetary-scale waves from the troposphere which break, dissipate and deposit easterly momentum
55 (Matsuno, 1971), although other factors such as stratospheric polar vortex (SPV) internal variability are also thought to be influential in determining the propensity for the occurrence of an SSW (de la Cámara et al., 2017; Scott and Polvani, 2006; White et al., 2019). The resulting enhanced poleward and downward transport during an SSW is also known to increase high-latitude stratospheric ozone (de la Cámara et al., 2018b; Hong and Reichler, 2021; Bahramvash Shams et al., 2022), and lead

to a breakdown of the SPV mixing barrier that leads to a flattening of chemical species gradients (Manney et al., 2009a; 2009b; Tao et al., 2015).

Whilst the timescales involved in relating LMS ozone anomalies to anomalous stratospheric circulation changes are well documented (Kiesewetter et al., 2010; Albers et al., 2018), the detailed vertical structure of the changes in the composition of the LMS (relevant for radiative impacts) and the implications for stratosphere-troposphere exchange (STE) of ozone have however received little attention thus far. The sensitivity of tropospheric ozone to variations in the Arctic and North Atlantic Oscillations has been widely discussed (Li et al., 2002; Creilson et al., 2003; Duncan et al., 2004), but these variations were explained by purely tropospheric mechanisms. Several studies indeed provide evidence of modulation to STE during anomalous stratospheric regimes (Sprenger and Wernli, 2003; Lamarque and Hess, 2004; Creilson et al., 2005; Ordóñez et al. 2007; Hess and Lamarque, 2007; Hsu and Prather, 2009; Pausata et al., 2012), though a quantitative assessment specifically following event-focussed, extreme cases such as midwinter SSWs has been performed in very few cases. A recent study by Xia et al. (2023), however, provided evidence for an enhancement in Arctic surface ozone following the SSW during the 2020/21 winter, at least with respect to the preceding 2019/20 winter which was characterised by a strong SPV largely throughout, due to enhanced downward stratosphere-to-troposphere (STT) transport. The spatial coincidence of positive surface ozone anomalies in midlatitudes, associated with cold air outbreaks in the weeks following this event, is highlighted as possible indication of SSW-driven enhancement in surface ozone, with directly implications for air quality.

Our goal here is to provide a more comprehensive and quantitative assessment of the influence of SSWs on LMS composition using state-of-the-art tools. To this end, the hindcast specified-dynamics reference (RefC1SD) simulation, nudged to ERA-Interim reanalysis, from the European Centre for Medium-Range Weather Forecasts – Hamburg (ECHAM)/Modular Earth Submodel System (MESSy) Atmospheric Chemistry (EMAC) chemistry-climate model (CCM) (1980–2013) is used to investigate changes in the chemical composition (both ozone and water vapour) over the Arctic (60–90° N), and over the mid-latitude continental regions. The EMAC model includes a detailed tropospheric chemistry scheme, with an on-line diagnostic to isolate and quantify the stratospheric influence on the troposphere, entailing the use of a stratospheric-tagged ozone (O_3S) tracer in which in situ tropospheric formation mechanisms are excluded (see Sect. 2.1 for more details). The model simulation was conducted specifically for the Chemistry Climate Model Initiative (CCMI-1) (Hegglin and Lamarque, 2015; Morgenstern et al., 2017). Evaluations conducted here of the model performance against both the Copernicus Atmospheric Monitoring Service (CAMS) reanalysis and ozone-sondes, in capturing chemical composition changes associated with SSWs, confirms the applicability of the EMAC model for such assessment.

An emphasis is placed on composition changes within the upper troposphere-lower stratosphere (UTLS) and troposphere, following events distinguished as either PJO or nPJO-type SSWs. This paper is organised as follows: details of the methods

performed are provided in Sect. 2, followed by an observational and reanalysis-based assessment to evaluate the high-latitude ozone and water vapour perturbation signal in EMAC in Sect. 3. This exercise is crucial to the investigation of the impact of SSWs on UTLS composition and STE of ozone, as the 35-year period (1979–2013) of the EMAC simulation used here yields a greater number of historical events than in the Copernicus Atmospheric Monitoring Service (CAMS) atmospheric composition reanalysis (2003-2022), which is necessary to obtain more statistically robust results. Distinction of SSW events into PJO and nPJO-type events, is then used to generate a composite evolution, averaged over all events during the 1980-2013 period, which is evaluated in Sect. 4. Here, the stratospheric-tagged ozone tracer (O_3S) is fundamental to the elucidation and quantification of the impact of SSWs on STE and subsequent enhancement in tropospheric ozone. In Sect. 5, the impacts on tropospheric ozone abundance over the major mid-latitude regions (North America, Europe and Asia) are statistically examined, including quantification of shifts in the likelihood of surface air quality exceedances. The radiative impacts of the simulated Arctic ozone and water vapour changes following PJO events, where the anomalies are much larger and more prolonged compared with nPJO events, are finally explored in Sect. 6. The findings are overall discussed in Sect. 7 and some key conclusions and identified next steps are outlined.

2 Data and Methods

2.1 Model description

The EMAC model is an interactively coupled state-of-the-art CCM. Variability in sea surface temperatures and sea ice concentration is accounted for from ERA-interim reanalysis data (Rayner et al., 2003; Jöckel et al. 2016; Morgernstern et al., 2017). The MACCity inventory, which is based on the Coupled Model Intercomparison Project Phase 5 inventory and Representative Concentration Pathway projections, is the source of prescribed decadal emissions of anthropogenic and natural greenhouse gas and ozone precursor emissions (which act as a forcing) (Lamarque et al., 2010; Brinkop et al., 2016; Jöckel et al. 2016), together with natural sources of variability that include volcanic eruptions and solar activity (Brinkop et al., 2016; Jöckel et al. 2016). Further detail of the model chemistry treatments and emission inventories may be found in Jöckel et al. (2016).

This study uses the hindcast specified-dynamics reference simulation (RC1SD-base-10) conducted for CCMI-1 for the period 1979–2013 (Hegglin and Lamarque, 2015; Morgenstern et al., 2017; Jöckel et al., 2020). We omit the first year from our evaluations to remove any influence from model spin-up effects in our evaluations. The prognostic variables of temperature, vorticity, divergence and (the logarithm of) surface pressure from the ERA-Interim reanalysis dataset are used for nudging the CCM towards the observed state of the atmosphere through Newtonian relaxation (nudging), with corresponding relaxation timescales of 24, 6, 48 and 24 h respectively (Jöckel et al., 2016). Model fields are output on a quadratic Gaussian grid which corresponds to a T42 (triangular) spectral resolution, equating to a horizontal spatial resolution of approximately 2.8°, and

contain 90 vertical hybrid sigma pressure levels up to 0.01 hPa (Jöckel et al., 2016). The ozone of stratospheric origin (O_3S)
120   model tracer is set to O_3 in the stratosphere and subject to the same sink reactions as ozone (O_3) in the troposphere but reactions
leading to the photochemical production of ozone are omitted for this tracer (Roelofs and Lelieveld, 1997; Jöckel et al., 2016).

2.2 Ozone-sondes

Vertical ozone profile data for the three long-running Arctic stations (Alert, Eureka and Ny-Ålesund) located poleward of
60°N, with measurements spanning at least 15 years of the 1980–2013 period (see Table 1 for details), was derived from the
125   World Ozone and Ultraviolet Radiation Data Centre database; this is an archive of balloon-borne in situ measurements of
ozone, together with other variables such as temperature, humidity, and pressure. Ozone-sondes typically provide a vertical
resolution of ~150 m from the surface up to a maximum altitude of approximately 35 km, although not in all cases (Worden
et al., 2007; Nassar et al., 2008). For the three selected Arctic stations, vertical ozone information is available on typically a
sub-weekly to weekly basis, but site-specific temporal recording inhomogeneities associated with instrumentation changes and
130   calibration issues (e.g., Fioletov et al., 2002) exist in the station records. The accuracy of ozone-sonde measurements is
typically estimated to be within the range of ±5 % in the troposphere (SPARC, 1998), depending on various factors. Precision
between different ozone-sonde types is estimated to be within ±3 %, with systematic biases of less than ±5 % within the lower
to middle stratosphere (12–27 km altitude range), provided that profile measurements have been normalised with respect to
ground-based total ozone measurements (SPARC, 1998).

135   **2.3 CAMS atmospheric composition reanalysis**

The Copernicus Atmospheric Monitoring Service (CAMS) dataset is the latest atmospheric composition reanalysis product
from the European Centre for Medium-Range Weather Forecasts (ECMWF), spanning the period 2003-2016 to date, which
now supersedes the earlier Monitoring Atmospheric Composition and Climate (MACC) and CAMS-interim reanalyses (Inness
et al., 2019). A reanalysis product objectively combines observations and numerical modelling to comprehensively simulate
140   weather and climate-related variables, based on a synthesised estimate of the state of the Earth's atmosphere. The development
and insights gained from the earlier datasets, enables the CAMS dataset to more accurately simulate the evolution of multiple
chemical species within the atmosphere, at enhanced horizontal (~80 km) and temporal resolution (3-hourly forecast fields
and hourly surface forecast fields). Smaller biases and greater temporal consistency are found in the CAMS simulated fields
of ozone (O_3), compared with that simulated by both MACC and CAMS-interim reanalyses; all of which are derived from
145   satellite observations assimilated into the numerical model (Inness et al., 2019).

2.4 Compositing procedures

For every time series, each nPJO and PJO SSW event (-30 to +150 days of an event) is indexed for inclusion in the composites
generated, and subsequently for each 30-day period analysed. We use Table 1 from Karpechko et al. (2017) to index all PJO

(n = 11)/nPJO (n = 11) events between 1980 and 2013 in our model simulations for inclusion in our composites. In calculating
150 the climatological composites, the indexing for each event is applied to all years, in calculating an average over the 34-year
time series (1980-2013). In examining regional shifts in mid-latitude ozone distributions (Sect. 5) and Arctic radiative impacts
(Sect. 6), however, the multi-year average is computed after all SSW cases (-30 to +150 days of an event) are removed from
each time series. This procedure removes any influence of seasonality in our evaluations.

2.5 Ozone distributions

155 Distributions of ozone for each region are calculated using a standard histogram binning approach for the subclass of SSW
events (n = 11) examined in Sect. 5. For each subcolumn, the integrated amount of ozone (in Dobson Units, DU) at every 10-
hourly model output timestep within each 30-day period (n = 72), multiplied by the number of model grid points in each
selected domain, is used in generating a histogram of the data (which is divided into 20 bins). This yields a total number of
data points of n = 392,040 for North America, n = 261,360 for Europe and n = 629,640 for Asia. The SSW and climatological
160 distributions (excluding SSW events as defined within -30 to +150 days of an event) are then compared. In determining the
statistical robustness of the results, a bootstrapping procedure involving resampling with replacement (Wilks, 2011) was
implemented (i.e., the original pool of values is used for every resample) to yield 95 % confidence intervals around the median,
90th percentile and 95th percentile of each distribution (Tables S1–S4 for O_3S and S5–S8 for the ozone (O_3) tracer). Each event
is considered to be an independent sample only (resulting in 11 SSW and 11 climatological cases) to remove any effects of
165 spatial and temporal autocorrelation. Bootstrapping was performed over a standard number of iterations (10000) to assign
confidence intervals and evaluate the extent to which the confidence intervals overlap. An additional common test of statistical
significance (two-sample t-test, with p <0.05) is performed separately in providing a thorough assessment.

2.6 Risk ratio (RR) calculation

The risk ratio (RR) of a 95-percentile exceedance in the ozone distributions following a PJO-type SSW, with respect to
170 climatology, is calculated for the three 30-day periods following the central warming (onset) date (lag 0: 0 to +30 days, lag 1:
+30 to +60 days and lag 2: +60 to +90 days) according to the approach by Zhang and Wang (2019, Fig. 1) in Sect. 5. From the
derived cumulative ozone distributions, the 95-percentile (0.95) level is identified for each climatological distribution at each
lag. The corresponding value of ozone (X_{ssw}, in DU) is used to identify the change in the proportion of the SSW distribution
above and below this 0.95 level. X_{ssw} is then used to determine the RR of an exceedance in ozone above this level as calculated
175 in Eq. 1:

$$RR = \frac{1 - X_{ssw}}{1 - 0.95} \tag{1}$$

The RR may also be calculated by substituting in a threshold value (e.g., the 60 ppbv ozone standard) in place of the 95th
percentile, when surface ozone values are considered.

2.7 Radiative impact calculations

180   A narrow-band radiative transfer code is used to calculate Fixed Dynamical Heating (FDH) stratospheric temperature changes due to ozone (O_3) and water vapour (H_2O) changes, following the method of Fels et al. (1980), using an updated version of the code described by Forster and Shine (1997). In the shortwave, O_3 absorption is represented at 5 nm resolution in the ultra-violet and 10 nm in the visible. Near-infrared absorption by H_2O is included in 14 spectral bands (Chagas et al., 2001). The longwave code employs a 10 cm^{-1} spectral resolution between 0 and 3000 cm^{-1} with updates described in Shine and Myhre

185   (2020); in addition to H_2O and O_3, present-day concentrations of carbon dioxide, nitrous oxide and methane are included. Calculations assume clear-sky conditions and solar insolation for 70° N on the 27th January (lag +10 day calculation) and 8th March (lag +50 day calculation). Day-averaged insolation is calculated using a 6-point Gaussian integration over the daylight hours. Both dates represent the mean lag date following the central warming (onset) date for all PJO-type SSW events (n = 11) during the period of the EMAC simulation (1980–2013). The FDH calculations are run to equilibrium and so may be

190   slightly larger in magnitude than transient FDH calculations (Forster et al., 1997). A composited polar-cap (60–90° N) mean temperature profile, at a lag of 10 (averaged between 5–15) and 50 (averaged between 45–55) days after the central warming date of a PJO-type SSW, was extracted from EMAC as input to these calculations. For a later set of idealised FDH calculations (Sect. 6.2), in determining the seasonal dependence of radiative impacts due to lower stratospheric O_3 and/or H_2O anomalies, an artificially induced perturbation (centred around 100 hPa), in which the five model levels above and below were adjusted

195   according to a quadratic function.

3 SSW chemical perturbation signal

Before investigating potential air quality and radiative impacts associated with PJO-type SSWs using EMAC, the associated signal of enhanced polar stratospheric ozone is first confirmed from ozone-sonde measurements. Over the last 9-year period of the EMAC simulation (2005–2013), overlapping with the CAMS reanalysis (excluding years 2003 and 2004 to remove any

200   impact of model spin-up effects in our evaluations), the agreement between the model and reanalysis time series of Arctic (60–90° N) ozone and water vapour is then quantified throughout the stratosphere-troposphere domain (1–1000 hPa). Such assessment is critical for deriving accurate interpretations of later results (Sect. 4 onwards).

3.1 Ozone

Figure 1a–c illustrates the poleward advection of anomalously high ozone which occurs during a PJO-type SSW onset, for the

205   January 2009 case which constituted the most intense and prolonged event on record (Manney et al., 2009a), in accordance with the splitting of the SPV and displacement of residual vortices equatorward. As indicated on each spatial map, calculated mean ozone-sonde profiles for the location of the three long-running high-latitude ozone-sonde monitoring stations detailed in Sect. 2.2 (representing climatological and SSW-impacted periods) are shown for the stratospheric dynamically active season

(which we take as December– to April inclusive) in Fig. 1d. Although the composited SSW-year profiles are well within the 1σ interval of non-SSW (climatological) years, a clear shift towards higher ozone is found throughout the profile, but particularly for each site at heights above ~350 hPa (mean tropopause height). Due to the sparse temporal sampling, such profiles have been composited over a full five-month period in which SSW impacts can occur, to yield a larger statistical sample. As such events likely only impact a shorter period of ~2–3 months, it is therefore expected that such approach may dilute the magnitude of the impact of the observed ozone enhancement, in connection with such events. We note that the shift between the two profiles overall increases slightly when only including the PJO-type SSWs during this period, with the greatest difference interestingly near the surface (Fig. S1). Whether this shift is physical (e.g., enhanced deep-STE events) or perhaps artificially inflated (e.g., due to temporal sampling bias) is an interesting question that merits further investigation on a case-study basis, although the small sample size of events inhibits such an assessment in a composite-based approach.

The signal for such ozone enhancement (and overall agreement) according to both CAMS and EMAC can be visualised in Fig. 2, following both two nPJO and four PJO events for the 2005–2013 period inclusive (a nine-year common baseline period for both datasets). The evolution in the deseasonalised ozone anomalies (%) is shown as function of pressure (height), encompassing the upper stratosphere down to the surface (1–1000 hPa), for the polar-cap (60–90° N) region. The 1–1000 hPa averaged Pearson correlation coefficient (r) over the whole period between each time series is 0.78, with values of between 0.86 and 0.94 between 10 and 300 hPa. Such values strongly support the notion that EMAC accurately simulates both interseasonal and interannual temporal variability in Arctic ozone abundance, particularly in the stratosphere; however, it is important to stress that CAMS does not constitute the truth (a detailed validation hindered by the sparse number of ozone-sonde stations poleward of 60°N). Overall, validation studies involving both ozone-sondes and aircraft measurements (e.g., MOZAIC-IAGOS) do however demonstrate that free tropospheric ozone (~350–750 hPa) is represented in CAMS to within an accuracy of ~±10 % (mean bias) throughout the year over mid-latitudes and the Arctic (Christophe et al., 2019). The agreement is higher still in the stratosphere as satellite observations are directly assimilated in this region. Nonetheless, Fig. 1d provides evidence to confirm the signal of an ozone enhancement over a longer historical timespan following such events.

Importantly, the key features of the evolution of the CAMS ozone anomalies in the stratosphere following the major PJO subclass of SSWs during the period, which notably includes the January 2009 and January 2013 vortex-split events, are well captured by EMAC. Moreover, EMAC-simulated variability in the evolution of stratosphere ozone anomalies during wintertime (the core of the stratospheric dynamically active season) in years without SSWs also closely resembles CAMS. Of note is the remarkable agreement and antisymmetric pattern to the anomalies for both the two major SSW events during this period, January 2009 and January 2013, with respect to the pronounced strong SPV during the 2010/11 winter (Manney et al., 2011). Whilst the key features of the stratospheric ozone anomaly evolution following each subclass of SSW are in agreement with other studies in the literature (e.g., de la Cámara et al., 2018b), this cannot be easily assessed here for the UTLS region due to differences in vertical coordinate system adopted (pressure versus isentropic surfaces), vertical domain and expression

of anomalies (% versus ppbv). An earlier evaluation from Kiesewetter et al. (2010, Fig. 7), derived using a chemistry transport model driven by sequentially assimilated solar backscatter UV (SBUV) satellite ozone profile observations, however, provides quantitative agreement to the findings here for multiple SSW events between 1979 and 2007 (>25 % anomalies in lower stratospheric polar ozone). Despite this, the lowermost isentropic surface assessed is 350 K (~150–200 hPa), so the agreement down to tropopause height (~320–330 K or 300–400 hPa) cannot be verified. The agreement between the CAMS reanalysis and the EMAC simulation, gives confidence the model performs well, particularly within the LMS (~100–300 hPa), with a time series correlation (r value) between 0.85 and 0.90 over the 2005–2013 period.

This EMAC-CAMS difference panel (Fig. 2c) shows that the correspondence between each dataset is very reasonable (typically <5 % difference) around and just after the SSW dates during the 2005–2013 period (vertical solid lines). Following the January 2009 event, EMAC does suggest ozone values of up to 10 % greater than CAMS in the lower stratosphere, although the anomaly using CAMS is still >25 % relative to climatology in the LMS (~100-300 hPa). The greatest disparity between the CAMS reanalysis and the EMAC simulation in the troposphere is evident during the summer of 2009, and from spring 2010 to the end of 2011, which did not coincide with any SSW occurrences. The evolution of the anomalies following the January 2013 SSW is however less consistently simulated between each dataset, although this is likely to be attributed to a change in the assimilated SBUV-2 data for ozone in the CAMS reanalysis from this year onwards (Christophe et al., 2019), resulting in a known discontinuity within the CAMS record. The disparity is largest in the troposphere, which although may seem counterintuitive, is highly likely related to propagation effects from the change in stratospheric assimilated information from the SBUV-2 platform, since no direct information on the vertical distribution of ozone in the troposphere region is assimilated into the reanalysis (Inness et al., 2019).

3.2 Water vapour

Figure 3 shows the temporal correspondence between EMAC and CAMS in the polar-cap averaged (60–90° N), vertically resolved (1–1000 hPa) deseasonalised water vapour (H_2O) anomalies (%), spanning the 2005–2013 period. A very high overall agreement in each time series for the stratosphere and troposphere combined is indicated by a Pearson correlation coefficient (r) value of 0.81 (averaged between 1 and 1000 hPa), which is higher than for that computed for ozone. Such value masks very large variations with pressure (height), with values of ~0.7 at both 10 and 150 hPa, reducing to <0.5 in between at 50 hPa, and falling to as low ~0.24 at 250 hPa. An r of ~0.0 was computed close to the stratopause (~1 hPa). This contrasts, with consistently high values of >0.9 in the troposphere between 400 and 1000 hPa.

The weaker correlation for the stratosphere can likely be related to the fact that H_2O is not assimilated in CAMS above the tropopause (~100–300 hPa), beneath which specific humidity is assimilated from radiosondes, dropsondes and aircraft observations (Hersbach et al., 2020); instead relatively simplistic parameterisation of oxidation from methane, that is directly

275 assimilated from satellite observations from multiple sources (SCIAMACHY, TANSO and IASI) (Massart et al., 2014), used for the representation of H_2O. Furthermore, it is quite widely established that reanalyses are notoriously poor at accurately simulating H_2O within the extratropical UTLS, due to deficiencies in the simulation of cross-tropopause mixing, and often positively biased (too moist) (Davis et al., 2017). It is therefore reasonable to assume that EMAC has a better handle over the spatiotemporal variability of this species.

280

The 50 hPa level (indicated by the upper horizontal dashed line) appears throughout much of the time period to be close to an inflexion point in which the sign of H_2O anomalies are opposite above and below this region. Thus, a slight deviation in the height of this critical layer or subtle timing differences in the onset of anomaly changes between the CAMS reanalysis and the EMAC simulation may account for the reduced correspondence at this level. This is even more true for the 200 hPa level

285 (lower horizontal dashed line), which is frequently close to the boundary between anomalously moist and dry conditions, particularly during winter. A dipole in this region is a common feature throughout the 9-year (2005–2013) period, with anomalies sometimes exceeding ±25 %. Following the major PJO-type SSWs over this period, which includes January 2006, January 2009 and January 2013, an anomalously dry region is found for heights above 200hPa, which overrides an anomalously moist region immediately below this level. It should be noted that this signal is not so pronounced following the other major

290 PJO-type event (February 2010) during this period according to either EMAC or the CAMS reanalysis. This pattern is not consistent with the nPJO subclass of SSW events during this period (February 2007 and February 2008), nor other winters during this period such as in the 2010/11 winter which was characterised by an anomalously strong SPV. In the latter case, a particularly strong H_2O dipole anomaly is present, with the sign of the anomalies inverted with respect to three of the PJO-type SSWs (January 2006, January 2009 and January 2013). The fundamental reasons for the occurrence of a dipole in this

295 region, which is most prevalent during winter, are unclear, but most likely relate to a vertical displacement in the mean tropopause height over the Arctic region and/or changes in poleward advection of moisture-rich air masses from lower latitudes.

4 Chemical perturbations in the tropopause region

Having verified that the EMAC simulated evolution in Arctic ozone and water vapour closely resemble the ozone-sonde and

300 CAMS reanalysis (Fig. 2 and 3), with the caveat that agreement between the model and CAMS is lower below the tropopause, we use EMAC to examine composition changes during SSWs for the 1980–2013 period to obtain more robust statistics through the inclusion of more events.

4.1 SSW chemical composition evolution

Figure 4a–c shows the composite evolution of deseasonalised anomalies (%) of ozone (O_3), water vapour (H_2O) and the vertical
residual velocity ($\overline{w}^*$), a metric for changes in the strength of polar downwelling (where downwelling is indicated by negative
$\overline{w}^*$), from the upper stratosphere to the surface (1–1000 hPa) over the period 1980–2013, split into nPJO (n = 11) and PJO (n
= 11) events[1]. The temperature composites for both nPJO and PJO events are shown in Fig. S2. The relative anomalies in both
O_3 and H_2O are more pronounced and protracted during PJO-type events, consistent with the resultant larger perturbation to
the dynamical state of the lower and middle stratosphere (Hitchcock et al., 2013). The onset (taken as the central warming date
denoted by the black solid lines in Fig. 4) of a PJO-type SSW is characterised by the emergence of positive O_3 anomalies (~5–
20 %) in the middle and lower stratosphere (10–100 hPa), and in the upper stratosphere (1–3 hPa) just a few days later (ΔO_3
>25 %), which is well established from previous stratospheric ozone SSW composite analyses (de la Cámara et al., 2018b;
Haase and Matthes, 2019). A larger, more prolonged relative enhancement (ΔO_3 >25 % persisting for ~50 days) is seen in the
LMS (tropopause to 100 hPa), which has so far received little attention. Concurrently, significant anomalies in H_2O are found
around the time of the SSW onset, largely confined to the LMS region, which last for around 50–70 days. A clear drying signal
(~25 %) is evident around 120-200 hPa, with a moistening signal of approximately equal magnitude immediately below, just
above the tropopause (~200–350 hPa). Only a modest enhancement of up to ~10 % in O_3 and ~±10 % in H_2O is evident
following nPJO events.

The long persistence timescales of the composition anomalies in the LMS reflect the dominant role of radiative processes, as
the reversal of the stratospheric winds suppresses the propagation of planetary-waves into the stratosphere (Hitchcock et al.,
2013). The evolution of polar downwelling ($\overline{w}^*$) anomalies show a period of accelerated descent throughout the Arctic
stratosphere immediately prior to an SSW in all cases. This is rapidly followed by a period of anomalously weak polar
downwelling in the upper stratosphere that gradually propagates down as the SSW evolves (in the case of PJO events). This
anomalous evolution in polar downwelling helps explain the establishment of the anomalies in O_3 and H_2O in the LMS and
perhaps also influences their persistence, but this aspect would need to be studied further. The persistence of such simulated
changes in composition are consistent with the delayed recovery of the SPV for PJO events, which are known to have larger
impacts on the tropospheric circulation (Hitchcock et al., 2013; de la Cámara et al., 2018a). Although an increase in
tropospheric ozone is shown during these events, the lack of statistical significance leads us to next further attempt to isolate
the stratospheric influence.

---

[1] An SSW event on 17 Feb 2002 is excluded in the nPJO/PJO classification in Karpechko et al. (2017).

4.2 Impact on stratosphere-to-troposphere exchange (STE) of ozone

To elucidate whether STE of ozone is enhanced as a result of the anomalous enrichment in LMS ozone, we use an additional model tracer which tracks only ozone of stratospheric origin (O_3S). We also derive and explore changes in the evolution of the tropospheric fraction of ozone of stratospheric origin (O_3F) using this tracer ($O_3F = O_3S/O_3$ x 100). The deseasonalised anomaly

335 (%) evolution for O_3S and O_3F are shown for both the nPJO and PJO-type event distinction (Fig. 5). A signal for enhanced STE is apparent for ~0–80 days following an SSW, although the entrainment of enhanced O_3S into the troposphere is initially confined to the upper troposphere (300–500 hPa). Deeper penetration of O_3S into the troposphere, and more clearly shown in the anomalies of O_3F, is evident from around 20 days after the SSW central warming date, extending out to ~80 days. Given a photochemical lifetime of ozone in the free troposphere around 3 weeks (Lelieveld et al., 2009) and a statistically significant

340 negative Arctic Oscillation pattern at least following PJO-type events (Hitchcock et al., 2013), favouring net equatorward transport in the troposphere, such a prolonged signal for elevated O_3S in the lower troposphere can only be attributable to enhanced STE for a sustained period (note that this tracer is subject to the same chemical sink reactions as the full ozone field).

For both composites, a peak response around 50 days after the SSW onset date is apparent, with indication of an enhancement

345 in O_3S throughout the troposphere and elevated near-surface O_3S which may impact air quality (see Sect. 5). The maximum increase in O_3S is on the order of ~5–10 % for PJO-type events, particularly near the surface, which equates to a change in the fraction of stratospheric ozone (O_3F) of >5 %. For this subset of events, the mean SSW onset date (17th January) is sufficiently early that this enhancement typically occurs when >50 % of tropospheric ozone is sourced from the stratosphere, at least initially. In contrast, a minimal enhancement of O_3F (~1–2 %) for a much shorter duration is shown to follow nPJO events,

350 which is even less significant as the fraction of ozone originating from the stratosphere is climatologically smaller (~30-50 %) just a few weeks later (mean nPJO event onset date: 11th February) as winter transitions to spring. These findings support the notion that SSWs exert a downward influence not only dynamically on tropospheric circulation (Baldwin and Dunkerton, 1999; Scaife et al., 2016), but also chemically on tropospheric composition, but primarily the PJO-type events. The delay of this influence by 50–80 days after the SSW onset ensures a maximum impact extending into the photochemically active season

355 (spring) (Logan, 1985; Lelieveld and Dentener, 2000). As shown in Williams et al. (2019), the seasonal peak in lower tropospheric O_3F over the Arctic occurs in winter, despite a maximum in tropospheric ozone during spring (>50 ppbv), since the partition of ozone from the stratosphere (O_3S) is similar in both seasons (~20-30 ppbv) meaning O_3F is typically ~10 % less in spring (~40-50 %).

5 Mid-latitude tropospheric ozone enhancement

360 The level of tropospheric entrainment of anomalously high ozone values in the LMS following PJO-type events over the Arctic (60–90° N) region is next assessed using EMAC over the populated mid-latitude regions of the Northern Hemisphere; the

Commented [RW1]: Clim O3F mention

hemisphere in which STE is most pronounced (Holton et al., 1995). This investigation is particularly pertinent to understanding how such events may affect the propensity for infringements of surface air quality standards. Although EMAC has a coarse horizontal resolution (~2.8°), therefore precluding a detailed assessment, it is possible to gauge the likelihood and approximate magnitude of an increase in background tropospheric ozone, together with the associated risk enhancement of surface ozone exceedances above regulatory standards. The use of a fully interactive specified-dynamics ozone simulation, together with an accompanying stratospheric-tagged ozone (O_3S) tracer, makes it possible to isolate a downward-propagating signal in ozone separate from modulating tropospheric influences (of both dynamical and chemical origin). In this section, shifts in composited regional ozone distributions for both non-SSW (climatological) versus SSW-impacted years are examined at multiple lags following the event onset (central warming date) from the UTLS down to the surface, for the PJO subclass of events earlier identified. This analysis is then repeated in an idealised case to help further extract and quantify the signal in the ozone tracer, separate from potential confounding effects arising from the response of tropospheric dynamical and chemical processes, as well as the presence of any underlying temporal trends (e.g., driven by trends in ozone precursor emissions) in the dataset, with respect to the signal strength.

5.1 Regional ozone distribution shifts

To ascertain changes in LMS and tropospheric ozone following PJO-type SSWs over different mid-latitude (30–70° N) regions of the Northern Hemisphere (Europe, North America and Asia), where enhanced stratospheric influx has the potential to affect air quality, distributions of the integrated quantity of ozone (Dobson Units; DU) are calculated for different select subcolumns. We include the SSW (solid lines) and climatology (dashed lines) composite distributions, using the O_3S tracer, for the LMS (100-300 hPa), upper troposphere (300-500 hPa), an approximation for the planetary boundary layer (PBL) (900-1000 hPa) and the model surface level: averaged over the 0–30-day, 30–60-day, and 60–90-day period following the SSW central warming date (Fig. 6) (see methods Sect. 2.4 for details on composite construction). For completeness and to conduct a surface air quality impact evaluation, we replicate the analysis for the full ozone field (Fig. S3). We employ a bootstrapping (resampling with replacement) procedure (Wilks, 2011) to evaluate the statistical robustness of the differences between the SSW and corresponding climatological distributions, as well as conducting a paired two-sample t-test (results are shown in Tables S1–S4 and further details of the approach are included in Sect. 2.5). This analysis is repeated for the full ozone field (Tables S5–S8). We additionally calculate risk ratios (RR) (displayed values) of the likelihood of an exceedance of the 95th percentile for each SSW distribution (using Eq. 1), with respect to each corresponding climatological distribution at each lag. An exception is that used for the model surface level in the O_3 case (Fig. S3), where we also substitute in the 60 ppbv threshold in place of the 95th percentile for each region (as mentioned in Sect. 2.6).

A noticeable shift of the O_3S SSW distributions is apparent for the LMS over each region with respect to climatology (Fig. 6a), with a statistically significant (p <0.05) shift towards higher values in all cases pertaining to the median, 90th and 95th

percentile of each distribution (Table S1). Given the proximity to the stratosphere in this region, Fig. S3 reflects this shift to a nearly equal magnitude for the full ozone distributions and the statistical significance ($p < 0.05$) is again evident from Table S5. Ultimately, this confirms that the overall enhancement in ozone evident from the polar-cap composites (Fig. 4) indeed extends over mid-latitude regions following this subclass of events. A more stringent measure of statistical significance is to discern this only where the calculated 95 % confidence intervals, as calculated through the bootstrapping approach, do not overlap (e.g., Schenker and Gentelman, 2001; Payton et al., 2003) for each statistic in every case (Tables S1 and S5). Using this measure, the shift in the median, 90th and 95th percentiles is again significant in every case for Europe and in most cases for both, Asia and North America (the exceptions are mostly between 0 and 30 days when the impact of the SSW has likely yet to peak). As an additional metric to quantify change in the proportion of the distributions in exceedance of the 95th percentile according to climatology, RR values of between ~2.0 and 2.5 for Europe and Asia equate to a doubling or more in the frequency of grid point incidences above this threshold for both O_3S (Fig. 6a) and the full ozone tracer (Fig. S3a). Values between 1.5 and 1.75 for North America translate to a lesser 50–75 % increase, which still also constitutes a substantial shift.

The shift of ozone distributions in the upper troposphere (300-500 hPa) for both O_3S (Fig. 6b) and O_3 (Fig. S3b) are qualitatively consistent to those in the LMS (100–300 hPa), further confirming that more ozone from the stratosphere is entrained into the free troposphere following such events according to EMAC. Whilst the result is statistically significant for O_3S for the 60–90-day lag (Table S2), associated with a corresponding subcolumn increase of ~1–2 DU, the significance of the signal for O_3 is marginal. This is highlighted by the presence of overlap between the 95 % confidence intervals for each respective climatological and SSW distribution for each statistic bootstrapped over, despite largely contradictory suggestion from the two-sample t-test performed (p-values generally less than 0.05). A notable exception to this is for the 95-percentile statistic over North America during this period (Table S6). For both O_3S and O_3, however, the frequency of a 95-percentile exceedance in the SSW distributions nevertheless ranges between a 25 and 70 % increase relative to climatology, according to the calculated RR values in Fig. 6 for O_3S and Fig. S3 for O_3 respectively (values are very similar in both cases).

The enhancement signal remains discernible for the approximation of the PBL used (here defined as 900–1000 hPa; Fig. 6c), which is consistent with model estimates of the depth of this layer during winter/springtime (McGrath-Sprangler et al., 2015) and the model surface level (Fig. 6d) in the case of O_3S, but is largely indistinguishable for O_3 (Fig. S3c,d). Interestingly, a paired two-sided t-test applied to the distributions implies that such signal is statistically significant in all cases for O_3S (Tables S3 and S4); this also holds true in most cases where this is inferred according to when the 95 % confidence intervals do not overlap, except during the first 30-day lag period when the impact of such events would not be expected to yet manifest. It is particularly interesting to note that a statistically significant signal according to both measures, computed for all three statistics, is detectable following such subclass of events according to the EMAC model for both the 30–60-day and 60–90-day lag periods, whereas this was most apparent for the upper troposphere for the 60–90-day lag interval. This finding could reflect an earlier enhancement near the surface courtesy of deep STT transport events, in which the stratospheric influence is at a

maximum in late winter/early spring as reported by many studies (e.g., Stohl et al., 2003; Lefohn et al., 2012; Lin et al., 2012; Škerlak et al., 2014), versus a slower background ozone enhancement driven by the large-scale descent that would be detectable

430   only later (Lefohn et al., 2011). In contrast to the O_3S finding, statistical significance cannot be inferred using either measure in almost all cases for the O_3 tracer (Tables S7 and S8). As shown in Sect. 5.2, however, it is reasonable to conclude that other factors may dampen the overall, background signal for a near-surface ozone enhancement following such events (which are still only in part isolated when examining the O_3S tracer).

435   Focussing on the change in the median, 90th and 95th percentile values for the model surface level (volume mixing ratio units of ppbv), an increase of ~1.5 to 3 ppbv of O_3S amount would translate to a maximum ozone concentration increase of ~3-6 µg m^{-3}. This equates to ~5–10 % of the 2021 World Health Organisation (WHO) surface air quality standards, which are set at 60 µg m^{-3} or 30 ppbv for a mean 8-hour interval during the season of peak surface ozone concentration (WHO, 2021). RR values of a 95th percentile exceedance according to constructed climatology are calculated for each of the PBL (900-1000 hPa) and

440   model surface level to be, furthermore, very close to one in the case of the O_3 tracer but on the order of ~1.5 to 3 (50-150 % increase) for the O_3S tracer. This finding is certainly of note and likely of greater concern for the impact on surface air quality resulting from more localised, episodic events, although this requires further investigation using much higher resolution tools and datasets. We next attempt to further isolate the signal of a background enhancement in near-surface ozone by artificially separating out potential confounding influences that may dampen the signal when using the ozone tracer of EMAC.

445   **5.2 Signal in background near-surface ozone**

Despite our efforts to circumvent the issue of limited sample size (i.e., 11 PJO-type SSW events during the 1980–2013 period) using a statistical bootstrapping approach, the lack of a statistically significant impact on regional distributions of Northern Hemisphere mid-latitude lower tropospheric ozone is not an unexpected result when using the full ozone (O_3) tracer. Whilst the use of the stratosphere-tagged ozone (O_3S) tracer helped confirm and isolate the signal of enhanced stratospheric influence,

450   which is clearly robust according to both a paired two-sided t-test and bootstrapping approach employed here, it is more meaningful to be able to verify and quantify the signal for O_3. Aside from the caveat of using a coarse-resolution (~2.8°) simulation, it is possible to artificially separate the influence of potential confounding factors, which give rise to the inherently large variability in tropospheric ozone, in addition to possible underlying trends within the dataset, to further extract the signal. We explore this by first subtracting the O_3S partition from the full ozone amount for the SSW composites, leaving the residual

455   amount of tropospheric-origin ozone, and then add the O_3S partition from the constructed climatological composites (non-SSW years), in creating a set of 'pseudo' climatological ozone distributions. Figure 7 shows the results of comparing these artificially constructed ozone distributions relative to composited SSW distributions for each region (North America, Europe and Asia), again for each lag: 0–30 days, 30–60 days and 60–90 days for the PBL (900–1000 hPa subcolumn) and model surface level.

460

The result Is that when using this method to create 'pseudo' climatological composites which are temporally consistent with the event occurrence dates (i.e., both SSW and climatological constructed composites contain the same amount of ozone derived from tropospheric production sources), the shift in each ozone distribution is more pronounced. This highlights that the enhanced stratospheric influence signal, as confirmed using the O_3S tracer (Fig. 6) and tested for statistical robustness
465 (Tables S1–S4), is present within the EMAC full ozone field. As quantified using the risk ratio metric (Eq. 1) to assess the probability change in the exceedance of the 95-percentile (Fig. 7a–b) or the 60 ppbv threshold for the model surface level (Fig. 7c), the values are significantly larger than for the compositing method used in Sect. 5.1 when using the O_3 tracer (Fig. S3c– e) and are generally higher even with respect to the equivalent evaluation using O_3S (Fig. 6c–d).

470 In terms of the upper tail-end of each pair of distributions, the impact is most pronounced for the earliest lag (0–30 days) which might be expected as enhanced STT transport events are likely to occur sooner than any overall background enhancement into the free troposphere facilitated by slow overall descent, as mentioned previously. The latter would have a larger impact on the overall distribution as opposed to the upper tail-end. Whilst there are some significant differences in the risk ratio changes for each given lag between Europe and North America, typically a factor of 2 to 3 increase (or equivalent to a 100 to 200 %
475 increase) in the number of incidences above either the 95-percentile of the 'pseudo' climatological distributions (or 60 ppbv threshold additional for the model surface level), it is notable that the signal is much weaker for Asia (risk ratios between 1.5 and 2.0 or 150 and 200% increase for the surface level). Such regional disparity is not evident from either Fig. 6 or Fig. S3 and could therefore be explained as a result of fixing the proportion of ozone formed in the troposphere for each pair of distributions. However, the relative role of tropospheric processes (dynamical or chemical) that may attenuate the signal, with
480 respect to possible underlying trends in the data, cannot be assessed here, although more detailed investigation is warranted in this regard.

6 Radiative impacts of Arctic ozone and water vapour perturbations

The ozone (O_3) and water vapour (H_2O) anomalies associated with SSWs will furthermore have radiative impacts which are likely not well represented in present-day Numerical Weather Prediction (NWP) models, potentially limiting forecast skill of
485 the overall simulation and tropospheric response to such events. In the case of ozone, many NWP models generally adopt a zonal-mean, monthly-mean climatological representation within their radiation schemes, owing to both computational constraints and untested accuracy of any 3D prognostic scheme performance (e.g., Monge-Sanz et al., 2022), although leading centres such as ECMWF are in the process of implementing this operationally in both NWP (10–15-day) and subseasonal forecasts (Williams et al., 2021). Whilst water vapour is much better represented in NWP models, particularly beneath the
490 tropopause, sharp discontinuities in the UTLS region are particularly troublesome to resolve and this is highly significant as this region is radiatively very sensitive (e.g., Riese et al., 2012; Shepherd et al., 2018). To explore and quantify such radiative

effects of composited perturbations in mean profile Arctic ozone and water vapour perturbations following PJO-type SSWs, calculations are performed for ~10 and 50 days after such events occur using the FDH technique (see Sect. 2.7). The radiative sensitivity of idealised UTLS ozone and water vapour perturbations over the Arctic is also investigated, through evaluating

495   results of a series of evaluations at key intervals during the stratospheric dynamically active season (December–April).

6.1 SSW radiative impacts

We calculate the radiatively-driven component of stratospheric temperature changes by performing FDH calculations for the subset of PJO-type SSW events (n = 11) during the period 1980-2013 using the EMAC model results. Figure 8 shows the polar-cap (60–90° N) mean O_3 and H_2O anomaly profiles (1–1000 hPa) averaged 5–15 days and 45–55 days after the central

500   warming (onset) date, together with the calculated FDH temperature changes (ΔT), due to each species separately and the total change. Note that the calculations are performed for profile averaged O_3 and H_2O over a 10-day interval to remove any impact of daily fluctuations which can be large, particularly during the early stages of such an event. The most significant temperature changes after the SSW onset (Fig. 8a–b) are found to occur in the LMS (tropopause to 100 hPa), in accordance with the largest changes in O_3 and H_2O with respect to climatology, as well as the high radiative sensitivity to composition changes in this

505   atmospheric region. A warming signal of ~1.5 K is evident around 150–200 hPa, mostly due to the reduction in H_2O, with a cooling signal centred around 250–300 hPa of ~2 K, induced by the perturbation to H_2O, but moderated slightly by the radiative warming effect of O_3 in this region. An enhancement of O_3 in the middle to lower stratosphere (10–100 hPa) results in a slight cooling (up to ~0.4 K), which is slightly offset by the radiative effect of H_2O (up to ~+0.1 K), leading to a net cooling of ~0.2– 0.3 K. This slight cooling, despite the increase in ozone at these levels, is mostly due to the change in upwelling longwave

510   radiation due to the larger (in percentage terms) increase in ozone in the lower stratosphere. This deprives the mid-stratosphere of upwelling infrared radiation which would otherwise warm this region; the reverse effect (where a lower stratospheric ozone depletion leads to cooling of the lower stratosphere but a warming of the mid-stratosphere) has been noted by Ramaswamy and Bowen (1994) and Shine (1996) for instance. Given this corresponds to late-January, changes in the longwave radiation budget will dominate over changes in the shortwave radiation budget. Above 10 hPa, O_3 changes alone lead to a cooling

515   tendency that increases with altitude (~>1 K at 1 hPa). The additional set of calculations averaged 45–55 days after the central warming (onset) date (Fig. 8c-d) yields similar results, indicating that such radiative effects, if ignored, would lead to a systematic temperature bias in NWP models, with possible knock-on consequences for wind fields. The ozone anomaly profile more closely matches the heating profile due to ozone throughout the stratosphere as solar insolation is much greater by early-March. We note that the heating effect due to ozone between 200 and 300 hPa is slightly larger for this later lag despite a

520   reduction in the percentage anomaly (from nearly 60 % to just under 40 %).

6.2 Idealised radiative impacts

The sensitivity of the lower stratospheric composition-induced modulation to the vertical profile in Arctic stratospheric temperature is next elucidated, as a function of both altitude and perturbation increment, during the evolution of the stratospheric dynamically active season (December–April). FDH-calculated changes in the mean polar-cap (60–90° N) vertical

525 temperature profile, resulting from an idealised perturbation in lower stratospheric (70–150 hPa) ozone and/or water vapour (see Sect. 2.7 for details), are shown in Fig. 9 with respect to the mid-December, mid-February and mid-April EMAC climatology (1980–2013). The increased radiative importance of ozone later in the season as solar input is greatly enhanced (increased short-wave heating) and slight reduction in the water vapour radiative effect is clearly evident. The opposing sign of the radiative effect from each constituent acts to offset the net temperature response to a varying degree within the UTLS.

530 Early in the season (December) however, water vapour exerts a dominant radiative control. This manifests in Fig. 9g as a warming of up to 3.5 K and a cooling of -3 K between ~70 and 150 hPa for an 80 % reduction and 100 % enhancement in both ozone and water vapour, respectively. The magnitude of this tendency gradually decreases with height above the 70 hPa level (upper bound of the perturbed region) as this region is only influenced by the non-local radiative effects. The tropopause region (~250 hPa) on the other hand is instead marked by an opposing radiative response (dipole) beneath this critical level (i.e., a

535 cooling and warming of up to ±3 K for an -80 % and a 100 % perturbation increment respectively). These tendencies are similar to Fig. 9h for mid-February, but the magnitude is reduced by an enhanced ozone radiative effect (Fig. 9b). For the mid-April case (Fig. 9i), the net radiative response between ~100 and 250 hPa is inverted (i.e., cooling for a reduction and a warming for an enhancement in both chemical species) as the radiative effect of ozone now overrides that of water vapour (evident in Fig. 9c and Fig. 9f).

540

Ranging from an 80 % reduction to a 100 % enhancement in both chemical constituents, the radiatively-driven temperature change is found to be largely linear with respect to the perturbation increment for each species. The net temperature response is thus mainly a product of the linear, additive radiative effects of ozone and water vapour combined, although an element of non-linearity becomes increasingly apparent for higher perturbation experiments. As well as both indirect (interactions from

545 both chemical agents) and non-local radiative mechanisms (i.e., the ΔT for each pressure level is determined by the ΔT for all other levels), such non-linearity can in part be attributed to the saturation effect of gaseous absorption at higher concentrations (the system is more sensitive to negative than positive perturbations of equal magnitude). This finding highlights the potential importance of radiative feedbacks between ozone and water vapour during stratospheric extreme events, such as the subset of PJO-type midwinter SSWs, when the vertical profile of ozone and water vapour abundance is most deviated relative to

550 climatology. Despite the greater complexity of the vertical profile perturbations in O_3 and H_2O, averaged both 10 and 50 days (corresponding to the 27th January and 8th March) after the composited event onset date (Fig. 8), the dipole response in temperature following a PJO-type SSW event is found to be highly consistent with that implied from the idealised sensitivity analysis for mid-February (Fig. 9b,e,h).

555 A caveat, by design, is that the FDH calculations do not provide temperature changes in the troposphere (300–1000 hPa), and cloud responses to the SSW (and any additional rapid tropospheric adjustments) are not accounted for, which may amplify or dampen the induced radiative forcing impact. The FDH calculations yield changes in radiative fluxes in the polar-cap due to the O_3 and H_2O changes which are of order +0.76 W m^{-2} at top of atmosphere, roughly equally due to the two gases and a change in surface radiative fluxes of -0.34 W m^{-2} due predominantly to O_3. These changes may be modulated by changes in

560 atmospheric and surface dynamics, clouds, tropospheric water vapour, as well as surface albedo, and their wider significance would need to be assessed in coupled-climate simulations (e.g., Deng et al., 2013).

7 Discussion

Using a specified-dynamics simulation (nudged to ERA-Interim) from the EMAC chemistry-climate model, along with observational evidence from the CAMS atmospheric composition reanalysis and ozone-sonde observations from three long-

565 running stations in the high Arctic, we show that the PJO subclass of midwinter SSWs (from a composite of 11 events between 1980–2013) are associated with significant composition changes in the polar UTLS that persist for extended timescales of up to 2-3 months. Despite significantly lower abundance of ozone in this region with respect to the mid-stratosphere (~10–30 hPa), positive anomalies in ozone of >25 % between 100 hPa and tropopause level are indeed highly significant as this has direct implications for STE of ozone, as well as residing in the atmospheric region of highest radiative sensitivity (Riese et al.,

570 2012). We show indication here that such events also lead to an enhancement in mid-latitude tropospheric ozone and the propensity for surface air quality exceedances above regulatory standards, in addition to radiative impacts which may affect NWP, up to 90 days following an event onset.

7.1 Air quality

For the subset of PJO-type events, the SSW-driven enhancement in lower stratospheric ozone is seen to subsequently propagate

575 into the troposphere on a timescale of 50-80 days over the Arctic region, with a statistically significant increase of ~5–10 % when using the ozone of stratospheric origin (O_3S) tracer to isolate the signal. In support of this finding, Xia et al. (2023) used Whole Atmosphere Community Climate Model version 6 (WACCM6) simulations to show that the Arctic surface ozone was elevated by about 11.3 % (or 14.7 % for the model O_3S tracer) in the two months following the January 2021 SSW, relative to the preceding winter which was characterised by a notably strong SPV. Our composite-based approach here, however, serves

580 to elucidate the importance of downward-propagating (PJO) versus largely non downward propagating (nPJO) events, and with respect to climatology, over multiple events in recent decades.

The signature for anomalously high levels of ozone in the LMS is confirmed in EMAC to extend across the continental mid-latitudes following such events, as is an enhanced downward flux of ozone into the troposphere through STE. Quantification using both the ozone (O_3) tracer and the O_3S tracer revealed a statistically robust signal in each case for the LMS, for each of the median, 90th and 95th percentile statistics when comparing the shifts in the regional distributions for multiple 30-day lag intervals following the mean event onset date (0–30, 30–60 and 60–90-day periods). This was found to be largely applicable in the upper troposphere down to the surface for O_3S in most cases, with the exception of the 0–30-day lag period according to the bootstrapped confidence interval overlap test. This finding is to be fully expected when considering the typical timeframe of downward-propagating dynamical influence of the extratropical troposphere. According to the risk ratio (RR) metric, used by Zhang and Wang (2019), the simulated number of incidences of an exceedance at the 95th percentile following such an event is on the order of a 50 to 150 % increase in O_3S with respect to climatology. This finding was not replicated when using the full ozone tracer initially, with an implied modest increase of less than 20 %.

We found indication that the much weaker signal using the ozone tracer near the surface (comparing Fig. 6c–d with Fig. S3c–d) was significantly impacted by confounding tropospheric factors. By fixing the amount of tropospheric ozone, in creating idealised ('pseudo') climatological composites, in which only the O_3S partition differs for each pair of regional ozone distributions (as in Fig. 7), it is clear that the ozone enhancement signal is much more pronounced. In terms of the RR metric, values were calculated to be at least as large (if not larger) as found for O_3S for both the PBL using the 95-percentile or the 60 ppbv threshold for the model surface level (up to a 200 % increase or a trebling in the risk of an exceedance). Tropospheric mechanisms that dampen the signal, of both dynamical and chemical origin, are effectively isolated using this method, as well as trends in ozone due to precursor emissions that are present in the 34-year period of the EMAC simulation. The issue with trends may in fact be more influential due to irregular temporal occurrence of the 11 PJO-type SSW events during this period (as shown in Table 1 of Karpechko et al., 2017), including a notable 10-year absence of any such events between winter 1988/89 and 1998/99. This evaluation highlights the importance of the compositing approach in isolating such signal. However, it remains to be seen if such signal is matched in the CAMS reanalysis, in which such assessment is hindered following our composite-based approach over a longer historical period, although this could be looked at on an individual event basis. It should be stressed that even a relatively small increase in the background enhancement of lower tropospheric ozone could translate to a significant increased risk of an exceedance above surface ozone air standards.

The coincidence of an increased risk of high surface ozone events during the springtime ozone maximum is of importance, as studies show that boundary layer processes (e.g., turbulent mixing) can entrain ozone with a stratospheric source origin well in excess of these air quality standards (Lefohn et al., 2011; Langford et al., 2017). Whilst our study indicates a possible larger impact on near-surface ozone levels for Europe and North America (relative to Asia) following such events, at least when compositing over all 11 identified PJO-type SSW events between 1980 and 2013 using EMAC, regional disparities may differ considerably between individual events (Lin et al., 2012; 2015). The results highlight both an increased background level of

tropospheric ozone over the Northern Hemisphere mid-latitude continents following this subclass of SSW events, lasting up to 90 days following the mean event onset, as well as perhaps an enhanced propensity for larger STT transport events relatively sooner that could impact near-surface ozone levels.

620

Such aspect concerns episodic, more localised events such as tropopause folding (the primary conduit in which STE occurs) that could contribute significantly to surface air quality exceedance events, which we attempt to highlight by closely examining the shift of the upper tail-end of each pair of distributions. However, such events are not simulated explicitly in EMAC as the associated mechanisms operate on sub-grid spatial scales. The question of whether more STT events follow PJO-type SSWs

625 (i.e., greater frequency of tropopause folding), or if such enhancement more directly associated with STT events is purely a result of entrainment of more ozone-enriched stratospheric air, cannot be assessed here but would be important to investigate. Ultimately, the choice of using the EMAC simulation here proved to be ideal for detecting a signal of enhanced background tropospheric ozone, as well as in highlighting the increased likelihood of surface air quality exceedances, over Northern Hemisphere mid-latitudes following this subclass of SSW events. Further investigation is next required using multiple, high

630 resolutions tools and datasets necessary to yield quantitative estimates on surface air quality impacts, in addition to investigate whether such a signal can be detected in observations, including networks of air quality monitoring stations.

Whilst Xia et al. (2023) noted a coincidence of high surface ozone spatial anomalies associated with mid-latitude cold-air outbreaks following the January 2021 SSW, a detailed stratospheric attribution assessment was not performed. To our

635 knowledge, our composite-based approach is the first such attempt to quantitatively attribute the role of midwinter SSWs on mid-latitude surface ozone, according to the subset of events which have a pronounced impact on the dynamical state of the lower stratosphere and indeed the troposphere.

7.2 Radiative impacts

Finally, with regard to the potential impact of UTLS composition anomalies on NWP forecast skill following such events,

640 typical perturbations in ozone and water vapour are found to significantly alter LMS temperatures, consistent with the known radiative sensitivity to UTLS composition perturbations (e.g., Randel and Wu, 2010; Riese et al., 2012; Gilford et al., 2016; Shepherd et al., 2018). The calculated UTLS temperature changes of ±2 K contribute to shortcomings in NWP models and hinder an accurate representation of dynamical downward coupling after an SSW (Domeisen et al., 2020; Friedel et al., 2022; Monge-Sanz et al., 2022). Most NWP models include only a simple representation of ozone chemistry (e.g., a zonal-mean

645 monthly climatology), whilst water vapour is problematic to resolve near the tropopause (e.g., issues in resolving numerical diffusion) and is not directly assimilated above the tropopause. Comparison of these findings with an identical number of nPJO-type events over this period highlights the much weaker signal for the subset of SSWs that are largely non-downward propagating, with minimal impacts upon the tropospheric circulation (Hitchcock et al., 2013; de la Cámara et al., 2018a).

Commented [RW2]: Look for couple of citations therein

Improved representation of composition changes resulting from SSWs could further enhance their role as a source of predictability on sub-seasonal to seasonal timescales, as shown in multiple event-specific evaluations in Sect. 4.4 of Williams et al. (2021) using forecast skill metrics such as the anomaly correlation coefficient. The findings here are of more direct relevance for the representation of stratosphere-troposphere coupling mechanisms which remain poorly understood.

Through evaluating the radiative impacts of idealised FDH calculations at key intervals during the stratospheric dynamically active season (December–April), in perturbing the abundance of lower stratospheric (70–150 hPa) ozone and/or water vapour, the timing of such an event occurrence is shown to impact the radiative impact following such events. The role of ozone (as a source of local short-wave heating) is negligible in early winter (i.e., mid-December) becoming significant by mid-February and dominant over the water vapour radiative contribution by mid-April. In contrast, the role of water vapour weakens slightly as the stratospheric dynamically active season unfolds, with a key inflexion point around 200 hPa (near tropopause height) for each of these three periods. Above this level, the radiative impact is opposite in sign with respect to ozone for either an induced negative (up to -80 %) or positive (up to 100 %) perturbation, but consistent beneath this level. The radiative response was found to be largely linear with perturbation increment and additive in calculating the net response.

The FDH calculations performed do not take into account dynamical adjustments such as due to cloud feedbacks, and thus serve only to highlight the radiative influence at different stages during Northern Hemisphere winter-spring. The unique character of each SSW event likely involves more complicated spatial structure, both geographically and with altitude, in UTLS ozone and water vapour anomalies. Nevertheless, the idealised results for a mid-February case here correspond closely with that computed for the PJO-type SSW composite case (for both a lag of 10 and 50 days following the mean event onset, which corresponds to the 27th of January and 8th March respectively). As shown in Table 1 by Karpechko et al. (2017), SSW events may however occur anytime between early winter into early spring, before the final warming or SPV breakdown, with the potential for radiative impacts due to resultant composition changes for at least 2 to 3 months after an event onset for the PJO subclass of events. We therefore conclude that associated changes in the chemical composition of the UTLS following PJO-type SSWs are likely to be of importance for NWP on sub-seasonal to seasonal timescales.

Acknowledgments

The lead author (R.S.W.) acknowledges PhD studentship funding from the SCENARIO NERC Doctoral Training Partnership Grant (NE/L002566/1). We acknowledge the work of the consortium of institutions that help to continuously develop the EMAC model. The EMAC simulation has been performed at the German Climate Computing Centre (DKRZ) through support from the Bundesministerium für Bildung und Forschung (BMBF). DKRZ and its scientific steering committee are gratefully acknowledged for providing the HPC and data archiving resources for this consortial project ESCiMo (Earth System Chemistry integrated Modelling).

Author Contributions

This research study was designed by R.S.W and M.I.H., with the manuscript written largely by R.S.W. under the close supervision of M.I.H. P.J. and H.G. led the development of the model simulations used in the analyses and provided technical support in relation to the specification of the various simulation results produced. K.P.S. performed the fixed dynamical heating calculations. All co-authors provided feedback which helped to improve the quality of the manuscript.

Competing Interests Statement

At least one of the (co-)authors is a member of the editorial board of Atmospheric Chemistry and Physics.

Data Availability

The EMAC model simulation results are freely and publicly available from the Climate and Environmental Retrieval and Archive (CERA) database at the German Climate Computing Centre (DKRZ; https://cera-www.dkrz.de/WDCC/ui/cerasearch/), the here analysed RC1SD-base-10 simulation under https://doi.org/10.26050/WDCC/RC1SD. The CAMS atmospheric composition reanalysis dataset can be downloaded freely from the ECMWF data catalogues (https://apps.ecmwf.int/data-catalogues/cams-reanalysis/?class=mc&expver=eac4). Ozone-sonde profile data can be accessed from the World Ozone and Ultraviolet Radiation Data Centre (WOUDC) (https://www.woudc.org, WMO/GAW Ozone Monitoring Committee, 2015).

Code Availability

Evaluation codes can be made available on request from R.S.W. and the fixed dynamical heating calculation code from K.P.S.

Corresponding Author

The corresponding author, Michaela I. Hegglin, can be contacted at m.i.hegglin@reading.ac.uk to answer any queries or requests for any materials associated with this research or direct these to the lead author (Ryan S. Williams).

References

Albers, J. R., Perlwitz, J., Butler, A. H., Birner, T., Kiladis, G. N., Lawrence, Z. D., Manney, G. L., Langford, A. O. and Dias, J.: Mechanisms Governing Interannual Variability of Stratosphere-to-Troposphere Ozone Transport, J. Geophys. Res-Atmos., 123, 234-260, https://doi.org/10.1002/2017JD026890, 2018.

705 Andrews D. G., Holton J. R., and Leovy C. B.: Middle Atmosphere Dynamics, Academic Press, San Diego, CA, ISBN 0—12 – 058576—6, 1987.

Bahramvash Shams, S., Walden, V. P., Hannigan, J. W., Randel, W. J., Petropavlovskikh, I. V., Butler, A. H., and de la Cámara, A.: Analyzing ozone variations and uncertainties at high latitudes during sudden stratospheric warming events using MERRA-2, Atmos. Chem. Phys., 22(8), 5435-5458, https://doi.org/10.5194/acp-22-5435-2022, 2022.

710 Baldwin, M. P., and Dunkerton, T. J.: Propagation of the Arctic Oscillation from the stratosphere to the troposphere, J. Geophys. Res-Atmos., 104, 30937-30946, https://doi.org/10.1029/1999JD900445, 1999.

Baldwin, M. P., and Dunkerton, T. J.: Stratospheric Harbingers of Anomalous Weather Regimes, Science, 294, 581-584, https://doi.org/10.1126/science.1063315, 2001.

Baldwin, M. P., Ayarzagüena, B., Birner, T., Butchart, N., Butler, A. H., Charlton-Perez, A. J., Domeisen, D. I. V., Garfinkel,

715 C. I., Garny, H., Gerber, E. P., Hegglin, M. I., Langematz, U., and Pedatella, N. M.: Sudden stratospheric warmings, Rev. Geophys., 59(1), e2020RG000708, https://doi.org/10.1029/2020RG000708, 2021.

Brinkop, S., Dameris, M., Jöckel, P., Garny, H., Lossow, S., and Stiller, G.: The millennium water vapour drop in chemistry–climate model simulations, Atmos. Chem. Phys., 16, 8125–8140, https://doi.org/10.5194/acp-16-8125-2016, 2016.

de la Cámara, A. D. L., Albers, J. R., Birner, T., Garcia, R. R., Hitchcock, P., Kinnison, D. E., and Smith, A. K., Sensitivity of

720 sudden stratospheric warmings to previous stratospheric conditions., J. Atmos. Sci., 74, 2857-2877, https://doi.org/10.1175/JAS-D-17-0136.1, 2017.

de la Cámara, A., Abalos, M., and Hitchcock, P.: Changes in stratospheric transport and mixing during sudden stratospheric warmings, J. Geophys. Res-Atmos. 123, 3356-3373, https://doi.org/10.1002/2017JD028007, 2018a.

725 de la Cámara, A., Abalos, M., Hitchcock, P., Calvo, N., and Garcia, R. R.: Response of Arctic ozone to sudden stratospheric warmings, Atmos. Chem. Phys., 18, 16499-16513, https://doi.org/10.5194/acp-18-16499-2018, 2018b.

Chagas, J., Newnham, D., Smith, K. and Shine, K.P.: Effects of improvements in near-infrared water vapour line intensities on short-wave atmospheric absorption, Geophys. Res. Lett., 28, 2401–2404, https://doi.org/10.1029/2000GL012412, 2001.

Charlton, A. J., Polvani, L. M., Perlwitz, J., Sassi, F., Manzini, E., Shibata, K., Pawson, S., Nielsen, J. E. And Rind, D.: A new

730 look at stratospheric sudden warmings. Part II: Evaluation of numerical model simulations, J. Climate, 20, 470-488, https://doi.org/10.1175/JCLI3994.1, 2007.

Christophe, Y., Bennouna, Y., Schulz, M., Eskes, H. J., Basart, S., Benedictow, A., Blechschmidt, A.-M., Chabrillat, S., Clark, H., Cuevas, E., Flentje, H., Hansen, K. M., Im, U., Kapsomenakis, J., Langerock, B., Petersen, K., Richter, A., Sudarchikova, N., Thouret V., Wagner A., Wang, Y., Warneke, T., and Zerefos, C.: Validation report of the CAMS global Reanalysis of

735 aerosols and reactive gases years 2003-2018, Copernicus Atmospheric Monitoring Service (CAMS) report, http://dx.doi.org/10.24380/dqws-kg08, 2019.

Creilson, J. K., Fishman, J., and Wozniak, A. E.: Intercontinental transport of tropospheric ozone: a study of its seasonal variability across the North Atlantic utilizing tropospheric ozone residuals and its relationship to the North Atlantic Oscillation, Atmos. Chem. Phys., 3, 2053–2066, https://doi.org/10.5194/acp-3-2053-2003, 2003.

740   Creilson, J. K., Fishman, J., and Wozniak, A. E.: Arctic Oscillation–induced variability in satellite-derived tropospheric ozone, Geophys. Res. Lett., 32, L14822, https://doi.org/10.1029/2005GL023016, 2005.

Davis, S. M., Hegglin, M. I., Fujiwara, M., Dragani, R., Harada, Y., Kobayashi, C., Long, C., Manney, G. L., Nash, E. R., Potter, G. L., Tegtmeier, S., Wang, T., Wargan, K. and Wright, J. S.: Assessment of upper tropospheric and stratospheric water vapor and ozone in reanalyses as part of S-RIP, Atmos. Chem. Phys, 17(20), 12743-12778, https://doi.org/10.5194/acp-17-

745   12743-2017, 2017.

Deng, Y., Park, T. W., and Cai, M.: Radiative and dynamical forcing of the surface and atmospheric temperature anomalies associated with the northern annular mode, J. Climate, 26, 5124-5138, https://doi.org/10.1175/JCLI-D-12-00431.1, 2013.

Domeisen, D. I., Sun, L., and Chen, G.: The role of synoptic eddies in the tropospheric response to stratospheric variability, Geophys. Res. Lett., 40, 4933-4937, https://doi.org/10.1002/grl.50943, 2013.

750   Domeisen, D. I., Butler, A. H., Charlton-Perez, A. J., Ayarzagüena, B., Baldwin, M. P., Dunn-Sigouin, E., and Taguchi, M.: The role of the stratosphere in subseasonal to seasonal prediction: 2. Predictability arising from stratosphere-troposphere coupling. J. Geophys. Res-Atmos., 125(2), e2019JD030923, https://doi.org/10.1029/2019JD030923, 2020.

Duncan, B. N., and Bey, I. A.: modeling study of the export pathways of pollution from Europe: Seasonal and interannual variations (1987–1997), J. Geophys. Res-Atmos., 109, D08301, https://doi.org/10.1029/2003JD004079, 2004.

755   Fels, S. B., Mahlman, J. D., Schwarzkopf, M. D., and Sinclair, R. W.: Stratospheric sensitivity to perturbations in ozone and carbon dioxide: Radiative and dynamical response, J. Atmos. Sci., 37, 2265–2297, https://doi.org/10.1175/1520-0469(1980)037<2265:SSTPIO>2.0.CO;2, 1980.

Fioletov, V. E., Bodeker, G. E., Miller, A. J., McPeters, R. D. and Stolarski, R.: Global and zonal total ozone variations estimated from ground-based and satellite measurements: 1964–2000, J. Geophys. Res-Atmos., 107(D22),

760   https://doi.org/10.1029/2001JD001350, 2022.

de F. Forster, P. M., Freckleton, R. S., and Shine K.P.: On the concept of radiative forcing, Clim. Dynam., 13, 547-560, https://doi.org/10.1007/s003820050182, 1997.

de F. Forster, P. M., and Shine K. P.: Radiative forcing and temperature trends from stratospheric ozone changes, J. Geophys. Res-Atmos., 102, 10841-10855, https://doi.org/10.1029/96JD03510, 1997.

765   Friedel, M., Chiodo, G., Stenke, A., Domeisen, D. I., Fueglistaler, S., Anet, J. G. and Peter, T.: Springtime arctic ozone depletion forces northern hemisphere climate anomalies. Nat. Geosci., 15(7), 541-547, https://doi.org/10.1038/s41561-022-00974-7, 2022.

Gilford, D. M., Solomon, S., and Portmann, R. W.: Radiative impacts of the 2011 abrupt drops in water vapor and ozone in the tropical tropopause layer, J. Climate, 29, 595-612, https://doi.org/10.1175/JCLI-D-15-0167.1, 2016.

770 Haase, S., and Matthes, K.: The importance of interactive chemistry for stratosphere–troposphere coupling, Atmos. Chem. Phys., 19, 3417-3432, https://doi.org/10.5194/acp-19-3417-2019, 2019.

Hegglin, M. I. and Lamarque, J.-F. and Eyring, V.: The IGAC/SPARC Chemistry-Climate Model Initiative Phase-1 (CCMI-1) model data output, NCAS British Atmospheric Data Centre, http://catalogue.ceda.ac.uk/uuid/9cc6b94df0f4469d8066d69b5df879d5, 2015.

775 Hersbach, H., Bell, B., Berrisford, P., Hirahara, S., Horányi, A., Muñoz-Sabater, J., Nicolas, J., Peubey, C., Radu, R., Schepers, D., Simmons, A., Soci, C., Abdalla, S., Abellan, X., Balsamo, G., Bechtold, P., Biavati, G., Bidlot, J., Bonavita, M., de Chiara, G., Dahlgren, P., Dee, D., Diamantakis, M., Dragani, R., Flemming, J., Forbes, R., Fuentes, M., Geer, A., Haimberger, L., Healy, S., Hogan, R. J., Hólm, E., Janisková, M., Keeley, S., Laloyaux, P., Lopez, P., Lupu, C., Radnoti, G., de Rosnay, P., Rozum, I., Vamborg, F., Villaume, S., and Thépaut, J.-N., The ERA5 global reanalysis, Q. J. Roy. Meteor. Soc., 146(730),

780 1999-2049, https://doi.org/10.1002/qj.3803, 2020.

Hess, P. G., and Lamarque, J.F.: Ozone source attribution and its modulation by the Arctic oscillation during the spring months, J. Geophys. Res-Atmos., 112, https://doi.org/10.1029/2006JD007557, 2007.

Hitchcock, P., Shepherd, T. G., and Manney, G. L.: Statistical characterization of Arctic polar-night jet oscillation events, J. Climate, 26, 2096-2116, https://doi.org/10.1175/JCLI-D-12-00202.1, 2013.

785 Holton, J. R., Haynes, P. H., McIntyre, M. E., Douglass, A. R., Rood, R. B., and Pfister, L.: Stratosphere-troposphere exchange, Rev. Geophys., 33(4), 403-439, https://doi.org/10.1029/95RG02097, 1995.

Hong, H.-J., and Reichler, T.: Local and remote response of ozone to Arctic stratospheric circulation extremes. Atmos. Chem. Phys., 21(2), 1159-1171, https://doi.org/10.5194/acp-21-1159-2021, 2021.

Hsu, J., and Prather, M. J.: Stratospheric variability and tropospheric ozone, J. Geophys. Res-Atmos., 114, D06102,

790 https://doi.org/10.1029/2008JD010942, 2009.Inness, A., Ades, M., Agustí-Panareda, A., Barré, J., Benedictow, A., Blechschmidt, A.-M., Dominguez, J. J., Engelen, R., Eskes, H., Flemming, J., Huijnen, V., Jones, L., Kipling, Z., Massart, S., Parrington, M., Peuch, V.-H., Razinger, M., Remy, S., Schulz, M., and Suttie, M.: The CAMS reanalysis of atmospheric composition, Atmos. Chem. Phys., 19, 3515-3556, https://doi.org/10.5194/acp-19-3515-2019, 2019.

Jöckel, P., Tost, H., Pozzer, A., Kunze, M., Kirner, O., Brenninkmeijer, C. A. M., Brinkop, S., Cai, D. S., Dyroff, C., Eckstein,

795 J., Frank, F., Garny, H., Gottschaldt, K.-D., Graf, P., Grewe, V., Kerkweg, A., Kern, B., Matthes, S., Mertens, M., Meul, S., Neumaier, M., Nützel, M., Oberländer-Hayn, S., Ruhnke, R., Runde, T., Sander, R., Sander, R., Scharffe, D., and Zahn, A.: Earth System Chemistry Integrated Modelling (ESCiMo) with the Modular Earth Submodel System (MESSy) version 2.51, Geosci. Model Dev., 9, 1153–1200, https://doi.org/10.5194/gmd-9-1153-2016, 2016.

Jöckel, P., Tost, H., Pozzer, A., Kunze, M., Kirner, O., Brenninkmeijer, C. A. M., Brinkop, S., Cai, D. S., Dyroff, C., Eckstein,

800 J., Frank, F., Garny, H., Gottschaldt, K.-D., Graf, P., Grewe, V., Kerkweg, A., Kern, B., Matthes, S., Mertens, M., Meul, S., Neumaier, M., Nützel, M., Oberländer-Hayn, S., Ruhnke, R., Runde, T., Sander, R., Sander, R., Scharffe, D., and Zahn, A.: ESCiMo / CCMI: hindcast simulations with specified dynamics, ERA-Interim SSTs/SICs. 1979-2013, World Data Center for Climate (WDCC) at DKRZ, https://doi.org/10.26050/WDCC/RC1SD, 2020.

Karpechko, A. Y., Hitchcock, P., Peters, D. H., and Schneidereit, A.: Predictability of downward propagation of major sudden stratospheric warmings. Q. J. Royal Meteorol. Soc, 143, 1459-1470, https://doi.org/10.1002/qj.3017, 2017.

Kidston, J., Scaife, A. A., Hardiman, S. C., Mitchell, D. M., Butchart, N., Baldwin, M. P., and Gray, L. J.: Stratospheric influence on tropospheric jet streams, storm tracks and surface weather, Nature Geosci., 8, 433-440, https://doi.org/10.1038/ngeo2424, 2015.

Kiesewetter, G., Sinnhuber, B. M., Vountas, M., Weber, M., and Burrows, J. P.: A long-term stratospheric ozone data set from assimilation of satellite observations: High-latitude ozone anomalies, J. Geophys. Res-Atmos., 115, D10307, https://doi.org/10.1029/2009JD013362, 2010.

Kolstad, E. W., Breiteig, T., and Scaife, A. A.: The association between stratospheric weak polar vortex events and cold air outbreaks in the Northern Hemisphere. Q. J. Roy. Meteor. Soc. 136, 886-893, https://doi.org/10.1002/qj.620, 2010.

Kretschmer, M., Cohen, J., Matthias, V., Runge, J., and Coumou, D.: The different stratospheric influence on cold-extremes in Eurasia and North America, Npj. Climat. Sci., 1, 44, https://doi.org/10.1038/s41612-018-0054-4, 2018a.

Kretschmer, M., Coumou, D., Agel, L., Barlow, M., Tziperman, E., and Cohen, J.: More-persistent weak stratospheric polar vortex states linked to cold extremes, Bull. Am. Meteorol. Soc., 99, 49-60, https://doi.org/10.1175/BAMS-D-16-0259.1, 2018b.

Lamarque, J. F., and Hess, P. G.: Arctic Oscillation modulation of the Northern Hemisphere spring tropospheric ozone, Geophys. Res. Lett., 31, L06127, https://doi.org/10.1029/2003GL019116, 2004.

Lamarque, J.-F., Bond, T. C., Eyring, V., Granier, C., Heil, A., Klimont, Z., Lee, D., Liousse, C., Mieville, A., Owen, B., Schultz, M. G., Shindell, D., Smith, S. J., Stehfest, E., Van Aardenne, J., Cooper, O. R., Kainuma, M., Mahowald, N., McConnell, J. R., Naik, V., Riahi, K., van Vuuren, D. P.: Historical (1850–2000) gridded anthropogenic and biomass burning emissions of reactive gases and aerosols: methodology and application, Atmos. Chem. Phys., 10, 7017–7039, https://doi.org/10.5194/acp-10-7017-2010, 2010.

Langford, A. O., Alvarez, R. J., Brioude, J., Fine, R., Gustin, M. S., Lin, M. Y., Marchbanks, R. D., Pierce, R. D., Sandberg, S. P., Senff, C. J., Weickmann, A. M., and Williams, E. J.: Entrainment of stratospheric air and Asian pollution by the convective boundary layer in the southwestern US, J. Geophys. Res-Atmos., 122, 1312-1337, https://doi.org/10.1002/2016JD025987, 2017.

Lefohn, A. S., Wernli, H., Shadwick, D., Limbach, S., Oltmans, S. J., and Shapiro, M.: The importance of stratospheric–tropospheric transport in affecting surface ozone concentrations in the western and northern tier of the United States, Atmos. Environ., 45, 4845-4857, https://doi.org/10.1016/j.atmosenv.2011.06.014, 2011.

Lefohn, A. S., Wernli, H., Shadwick, D., Oltmans, S. J., and Shapiro, M.: Quantifying the importance of stratospheric-tropospheric transport on surface ozone concentrations at high-and low-elevation monitoring sites in the United States, Atmos. Environ., 62, 646-656, https://doi.org/10.1016/j.atmosenv.2012.09.004, 2012.

Lelieveld, J. and Dentener, F. J.: What controls tropospheric ozone?, *J. Geophys. Res.-Atmos., 105*, 3531-3551, https://doi.org/10.1029/1999JD901011, 2000.

Lelieveld, J., Hoor, P., Jöckel, P., Pozzer, A., Hadjinicolaou, P., Cammas, J. P., and Beirle, S.: Severe ozone air pollution in the Persian Gulf region. Atmos. Chem. Phys., 9(4), 1393-1406, https://doi.org/10.5194/acp-9-1393-2009, 2009.

840 Li, Q., Jacob, D. J., Bey, I., Palmer, P. I., Duncan, B. N., Field, B. D., Martin, R. V., Fiore, A. M., Yantosca, R. M., Parrish, D. D., Simmonds, P. G., and Oltmans, S. J.: Transatlantic transport of pollution and its effects on surface ozone in Europe and North America, J. Geophys. Res-Atmos., 107, 4166, https://doi.org/10.1029/2001JD001422, 2002.

Lin, M., Fiore, A. M., Cooper, O. R., Horowitz, L. W., Langford, A. O., Levy II, H., Johnson, B. J., Naik, V., Oltmans, S. J., and Senff, C. J.: Springtime high surface ozone events over the western United States: Quantifying the role of stratospheric

845 intrusions, J. Geophys. Res.-Atmos., 117, D00V22, https://doi.org/10.1029/2012JD018151, 2012.

Lin, M., Fiore, A. M., Horowitz, L. W., Langford, A. O., Oltmans, S. J., Tarasick, D., and Rieder, H. E.: Climate variability modulates western US ozone air quality in spring via deep stratospheric intrusions, Nat. Commun., 6, 7105, https://doi.org/10.1038/ncomms8105, 2015.

Logan, J. A.: Tropospheric ozone: Seasonal behavior, trends, and anthropogenic influence, J. Geophys. Res-Atmos., 90,

850 10463-10482, https://doi.org/10.1029/JD090iD06p10463, 1985.

Manney, G. L., Schwartz, M. J., Krüger, K., Santee, M. L., Pawson, S., Lee, J. N., Daffer, W. H., Fuller, R. A., and Livesey, N. J.: Aura Microwave Limb Sounder observations of dynamics and transport during the record-breaking 2009 Arctic stratospheric major warming, Geophys. Res. Lett., 36, L12815, https://doi.org/10.1029/2009GL038586, 2009a.

Manney, G. L., Harwood, R. S., Mackenzie, I. A., Minschwaner, K., Allen, D. R., Santee, M. L., Walker, K. A., Hegglin, M.

855 I., Lambert, A., Pumphrey, H. C., Bernath, P. F., Boone, C. D., Schwartz, M. J., Livesey, N. J., Daffer, W. H., and Fuller, R. A.: Satellite observations and modeling of transport in the upper troposphere through the lower mesosphere during the 2006 major stratospheric sudden warming, Atmos. Chem. Phys., 9, 4775–4795, https://doi.org/10.5194/acp-9-4775-2009, 2009b.

Manney, G. L., Santee, M. L., Rex, M., Livesey, N. J., Pitts, M. C., Veefkind, P., Nash, E. R., Wohltmann, I., Lehmann, R., Froidevaux, L., Poole, L. R., Schoeberl, M. R., Haffner, D. P., Davies, J., Dorokhov, V., Gernandt, H., Johnson, B., Kivi, R.,

860 Kyrö, E., Larsen, N., Levelt, P. F., Makshtas, A., McElroy, C. T., Nakajima, H., and Zinoviev, N. S.: Unprecedented Arctic ozone loss in 2011, Nature, 478(7370), 469-475, https://doi.org/10.1038/nature10556, 2011.

Massart, S., Agusti-Panareda, A., Aben, I., Butz, A., Chevallier, F., Crevosier, C., Engelen, R., Frankenberg, C., Hasekamp, O.: Assimilation of atmospheric methane products into the MACC-II system: from SCIAMACHY to TANSO and IASI, Atmos. Chem. Phys., 14, 6139-6158, https://doi.org/10.5194/acp-14-6139-2014, 2014.

865 Matsuno, T.: A dynamical model of the stratospheric sudden warming, J. Atmos. Sci., 28, 1479-1494, https://doi.org/10.1175/1520-0469(1971)028<1479:ADMOTS>2.0.CO;2, 1971.

McGrath-Spangler, E. L., Molod, A., Ott, L. E., and Pawson, S.: Impact of planetary boundary layer turbulence on model climate and tracer transport, Atmos. Chem. Phys., 15, 7269–7286, https://doi.org/10.5194/acp-15-7269-2015, 2015.

Monge-Sanz, B. M., Bozzo, A., Byrne, N., Chipperfield, M. P., Diamantakis, M., Flemming, J., Gray, L. J., Hogan, R. J.,

870 Jones, L., Magnusson, L., Polichtchouk, I., Shepherd, T. G., Wedi, N., and Weisheimer, A.: A stratospheric prognostic ozone

for seamless Earth system models: performance, impacts and future, Atmos. Chem. Phys., 22, 4277–4302, https://doi.org/10.5194/acp-22-4277-2022, 2022.

Monge-Sanz, B. M., Bozzo, A., Byrne, N., Chipperfield, M. P., Diamantakis, M., Flemming, J., and Weisheimer, A.: A stratospheric prognostic ozone for seamless Earth system models: performance, impacts and future. Atmos. Chem Phys., 22(7), 4277-4302, https://doi.org/10.5194/acp-22-4277-2022, 2022.

Morgenstern, O., Hegglin, M. I., Rozanov, E., O'Connor, F. M., Abraham, N. L., Akiyoshi, H., Archibald, A. T., Bekki, S., Butchart, N., Chipperfield, M. P., Deushi, M., Dhomse, S. S., Garcia, R. R., Hardiman, S. C., Horowitz, L. W., Jöckel, P., Josse, B., Kinnison, D., Lin, M., Mancini, E., Manyin, M. E., Marchand, M., Marécal, V., Michou, M., Oman, L. D., Pitari, G., Plummer, D. A., Revell, L. E., Saint-Martin, D., Schofield, R., Stenke, A., Stone, K., Sudo, K., Tanaka, T. Y., Tilmes, S., Yamashita, Y., Yoshida, K., and Zeng, G.: Review of the global models used within phase 1 of the Chemistry–Climate Model Initiative (CCMI), Geosci. Model Dev., 10, 639–671, https://doi.org/10.5194/gmd-10-639-2017, 2017.

Nakagawa, K. I., and Yamazaki, K.: What kind of stratospheric sudden warming propagates to the troposphere?, Geophys. Res. Lett., 33(4), L04801, https://doi.org/10.1029/2005GL024784, 2006.

Nassar, R., Logan, J. A., Worden, H. M., Megretskaia, I. A., Bowman, K. W., Osterman, G. B., Thompson, A. M., Tarasick, D. W., Austin, S., Claude, H., Dubey, M. K., Hocking, W. K., Johnson, B. J., Joseph, E., Merrill, J., Morris, G. A., Newchurch, M., Oltmans, S. J., Posny, F., Schmidlin, F. J., Vömel, H., Whiteman, D. N., and Witte, J. C.: Validation of Tropospheric Emission Spectrometer (TES) nadir ozone profiles using ozonesonde measurements, J. Geophys. Res.-Atmos., 113, D15S17, https://doi.org/10.1029/2007JD008819, 2008.

Ordóñez, C., Brunner, D., Staehelin, J., Hadjinicolaou, P., Pyle, J. A., Jonas, M., Wernli, H., and Prévôt, A. S.: Strong influence of lowermost stratospheric ozone on lower tropospheric background ozone changes over Europe, Geophys. Res. Lett., 34, L07805, https://doi.org/10.1029/2006GL029113, 2007.

Pausata, F. S. R., Pozzoli, L., Vignati, E., and Dentener, F. J.: North Atlantic Oscillation and tropospheric ozone variability in Europe: model analysis and measurements intercomparison, Atmos. Chem. Phys., 12, 6357-6376, https://doi.org/10.5194/acp-12-6357-2012, 2012.

Payton, M. E., Greenstone, M. H. and Schenker, N.: Overlapping confidence intervals or standard error intervals: what do they mean in terms of statistical significance?, J. Insect Sci., 3(1), https://doi.org/10.1093/jis/3.1.34, 2003.

Randel, W. J., and Wu, F.: The polar summer tropopause inversion layer, J. Atmos Sci., 67, 2572-2581, https://doi.org/10.1175/2010JAS3430.1, 2010.

Rayner, N. A., Parker, D. E., Horton, E. B., Folland, C. K., Alexander, L. V., Rowell, D. P., Kent, E. C., and Kaplan, A.: Global analyses of sea surface temperature, sea ice, and night marine air temperature since the late nineteenth century, J. Geophys. Res.-Atmos, 108, 4407, https://doi.org/10.1029/2002JD002670, 2003.

Riese, M., Ploeger, F., Rap, A., Vogel, B., Konopka, P., Dameris, M. and Forster, P.: Impact of uncertainties in atmospheric mixing on simulated UTLS composition and related radiative effects, J. Geophys. Res-Atmos, 117, D16305, https://doi.org/10.1029/2012JD017751, 2012.

905 Roelofs, G. J., and Lelieveld, J. O. S.: Model study of the influence of cross-tropopause O3 transports on tropospheric O3 levels., Tellus B, 49, 38-55, https://doi.org/10.3402/tellusb.v49i1.15949, 1997.

Scaife, A. A., Karpechko, A. Y., Baldwin, M. P., Brookshaw, A., Butler, A. H., Eade, R., Gordon, M., MacLachlan, C., Martin, N., Dunstone, N., and Smith D.: Seasonal winter forecasts and the stratosphere, Atmos. Sci Lett., 17, 51-56, https://doi.org/10.1002/asl.598, 2016.

910 Schenker, N., and Gentleman, J. F.: On judging the significance of differences by examining the overlap between confidence intervals, Am. Stat., 55(3), 182-186, https://doi.org/10.1198/000313001317097960, 2001.

Scott, R. K., and Polvani, L. M.: Internal variability of the winter stratosphere. Part I: Time-independent forcing, J. Atmos. Sci., 63, 2758-2776, https://doi.org/10.1175/JAS3797.1, 2006.

Shine, K.P.: On the modelled thermal response of the Antarctic stratosphere to a depletion of ozone. Geophys. Res. Lett., 13, 915 1331-1334, https://doi.org/10.1029/GL013i012p01331, 1996.

Shepherd, T. G., Polichtchouk, I., Hogan, R. J., and Simmons, A. J.: Report on stratosphere task force. European Centre for Medium-Range Weather Forecasts. ECMWF Technical Memorandum, 824, https://doi.org/10.21957/0vkp0t1xx, 2018.

Shine, K. P., and Myhre, G.: The spectral nature of stratospheric temperature adjustment and its application to halocarbon radiative forcing, J. Adv. Model. Earth Sy., 12(3), e2019MS001951, https://doi.org/10.1029/2019MS001951, 2020.

920 Sigmond, M., Scinocca, J. F., Kharin, V. V. and Shepherd, T. G.: Enhanced seasonal forecast skill following stratospheric sudden warmings, Nature Geosci., 6, 98-102, https://doi.org/10.1038/ngeo1698, 2013.

Škerlak, B., Sprenger, M., and Wernli, H.: A global climatology of stratosphere–troposphere exchange using the ERA-Interim data set from 1979 to 2011. Atmos. Chem. Phys., 14(2), 913-937, https://doi.org/10.5194/acp-14-913-2014, 2014.

SPARC, SPARC/IOC/GAW Assessment of Trends in the Vertical Distribution of Ozone, edited by: Harris, N., Hudson, R., 925 and Phillips, C., SPARC Report No. 1, WMO Ozone Research and Monitoring Project Report No. 43, https://www.sparc-climate.org/publications/sparc-reports/sparc-report-no-1/, 1998.

Sprenger, M., and Wernli, H.: A northern hemispheric climatology of cross-tropopause exchange for the ERA15 time period (1979–1993), J. Geophys. Res-Atmos., 108, 8521, https://doi.org/10.1029/2002JD002636, 2003.

Stohl, A., Spichtinger-Rakowsky, N., Bonasoni, P., Feldmann, H., Memmesheimer, M., Scheel, H. E., Trickl, T., Hübener, S., 930 Ramaswamy, V., and Bowen, M. M.: Effect of changes in radiatively active species upon the lower stratospheric temperatures, J. Geophys. Res., 99(D9), 18909–18921, https://doi.org/10.1029/94JD01310, 1994.

Ringer, W., Mandl, M.: The influence of stratospheric intrusions on alpine ozone concentrations, Atmos. Environ., 34(9), 1323-1354, https://doi.org/10.1016/S1352-2310(99)00320-9, 2000.

Tao, M., Konopka, P., Ploeger, F., Grooβ, J.-U., Müller, R., Volk, C. M., Walker, K. A., and Riese, M.: Impact of the 2009 935 major sudden stratospheric warming on the composition of the stratosphere, Atmos. Chem. Phys., 15, 8695-8715, https://doi.org/10.5194/acp-15-8695-2015, 2015.

Thompson, D. W., Baldwin, M. P., and Wallace, J. M.: Stratospheric connection to Northern Hemisphere wintertime weather: Implications for prediction, J. Climate, 15, 1421-1428, https://doi.org/10.1175/1520-0442(2002)015<1421:SCTNHW>2.0.CO;2, 2002.

940 White, I., Garfinkel, C. I., Gerber, E. P., Jucker, M., Aquila, V., and Oman, L. D.: The downward influence of sudden stratospheric warmings: Association with tropospheric precursors, J. Climate, 32, 85-108, https://doi.org/10.1175/JCLI-D-18-0053.1, 2019.

Wilks, D. S.: Statistical methods in the atmospheric sciences (Vol. 100), Academic press, 2011.

Williams, R. S., Hegglin, M. I., Kerridge, B. J., Jöckel, P., Latter, B. G., and Plummer, D. A.: Characterising the seasonal and
945 geographical variability in tropospheric ozone, stratospheric influence and recent changes, Atmos. Chem. Phys., 19, 3589–3620, https://doi.org/10.5194/acp-19-3589-2019, 2019.

Williams, R. S., Hogan, R. J., Polichtchouk, I., Hegglin, M. I., Stockdale, T., and Flemming, J. Evaluating the Impact of Prognostic Ozone in IFS NWP Forecasts. European Centre for Medium-Range Weather Forecasts. ECMWF Technical Memorandum, 887, https://doi.org/10.21957/rakfo1qo3, 2021.

950 Worden, H. M., Logan, J. A., Worden, J. R., Beer, R., Bowman, K., Clough, S. A., Eldering, A., Fisher, B. M., Gunson, M. R., Herman, R. L., Kulawik, S. S., Lampel, M. C., Luo, M., Megretskaia, I. A., Osterman, G. B., and Shephard, M. W.: Comparisons of Tropospheric Emission Spectrometer (TES) ozone profiles to ozonesondes: Methods and initial results, J. Geophys. Res.-Atmos., 112, D03309, https://doi.org/10.1029/2006JD007258, 2007.

World Health Organization (WHO), WHO global air quality guidelines: particulate matter (PM2.5 and PM10), ozone, nitrogen
955 dioxide, sulfur dioxide and carbon monoxide. World Health Organization, https://apps.who.int/iris/handle/10665/345329. License: CC BY-NC-SA 3.0 IGO., 2021.

Xia, Y., Xie, F., and Lu, X.: Enhancement of Arctic surface ozone during the 2020–2021 winter associated with the sudden stratospheric warming, Environ. Res. Lett., 18, 024003, https://doi.org/10.1088/1748-9326/acaee0, 2023.

Zhang, J., and Wang, F.: Changes in the Risk of Extreme Climate Events over East Asia at Different Global Warming
960 Levels. Water, 11, 2535, https://doi.org/10.3390/w11122535, 2019.

965
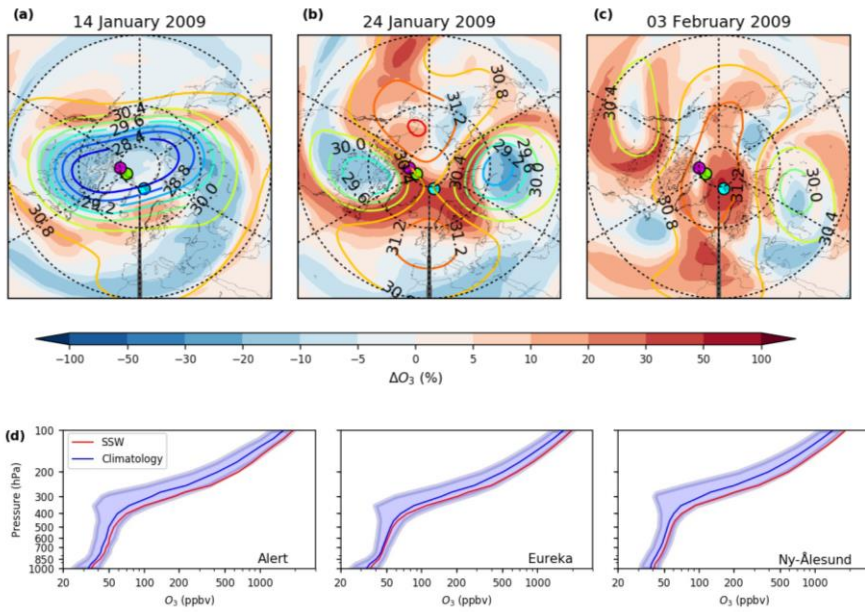
970

Figure 1: 10 hPa geopotential height (km) (contours) and deseasonalised ozone percentage anomalies (shading) over the Northern Hemisphere for (a) 10 days before, (b) the SSW central warming date and (c) 10 days after a split vortex, PJO-type SSW event (January 2009) from the CAMS atmospheric composition reanalysis. Ozone anomalies are calculated with respect to the 2005–2013 baseline period. Contour intervals are 0.4 km. (d) Ozone-sonde (100–1000 hPa) climatology and SSW composite profiles for three long-running Arctic sites: Alert (green circle), Eureka (violet circle) and Ny-Ålesund (cyan circle) as marked on each map in (a–c). Mean SSW profiles were composited from all profiles within 0 to +70 days of an SSW central warming date with all remaining profiles (excluding the 20 days prior to an event) used in compositing a mean climatology profile during the stratosphere dynamically active season (December-April). Blue shaded region represents 1σ around the climatological mean. The climatology is constructed excluding SSW events in each case.

975

980
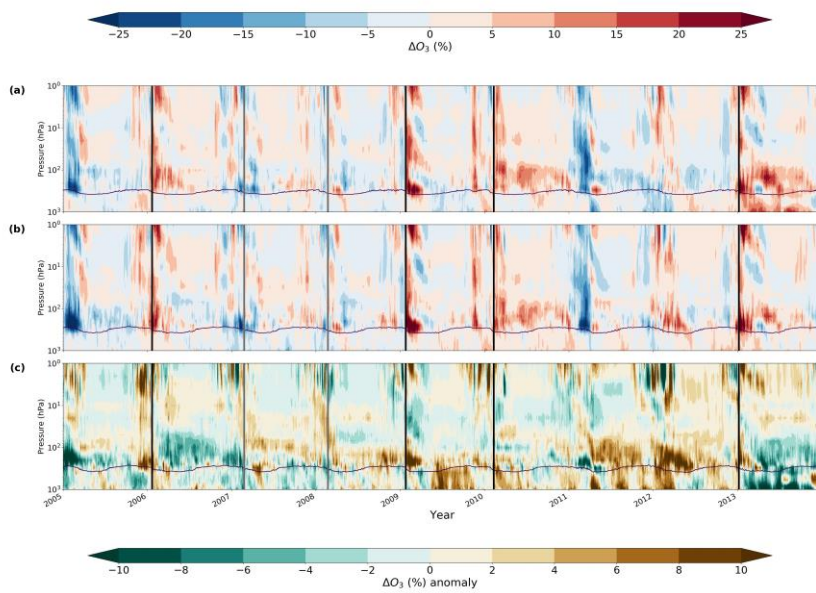
Figure 2: Vertical-time evolution of polar-cap (60–90° N) deseasonalised ozone (%) anomalies for (a) CAMS reanalysis and (b) from the EMAC CCM specified-dynamics simulations relative to each respective climatology over the period 2005–2013. The difference
985 **between each anomaly time series (EMAC – CAMS) is additionally shown in (c). Vertical black (grey) lines denote the subclass of PJO (nPJO) SSW central warming dates during the period. The 100 ppbv ozone contour (purple line) is included as a proxy for the tropopause pressure.**
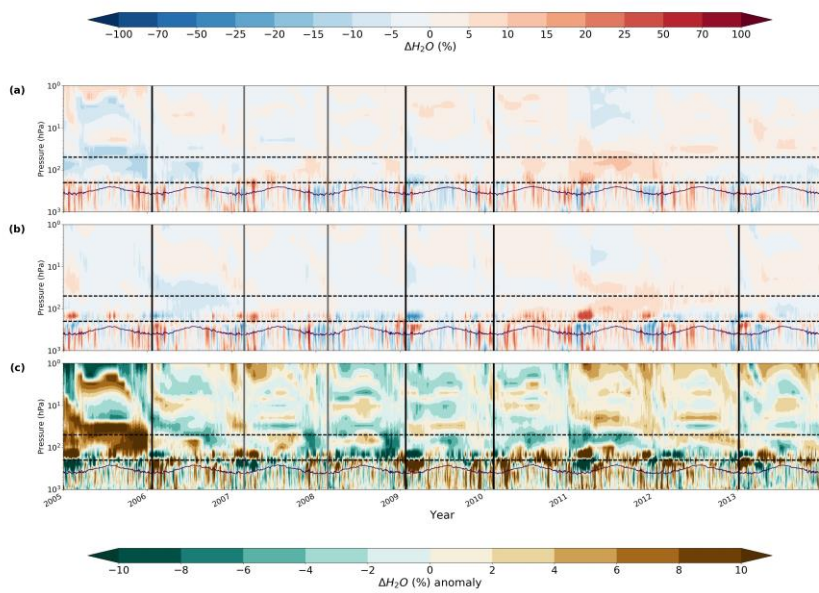
Figure 3: Same as Fig. 2 but for the vertical-time evolution of polar-cap (60–90° N) deseasonalised water vapour (%) anomalies. We additionally mark the 50 hPa and 200 hPa level (upper and lower dashed line respectively) to highlight common inflexion points between opposing sign anomalies, following some of the SSW events during this period (mostly notably the PJO-type events).
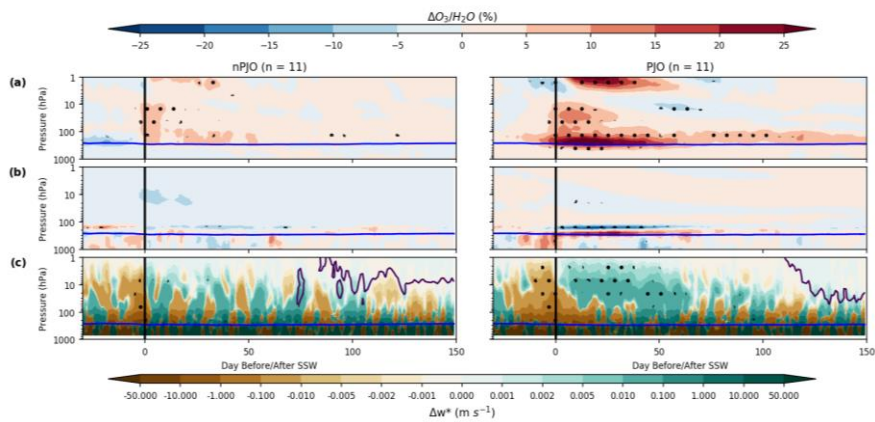
Figure 4: Vertical-time composites of polar-cap (60–90° N) averaged (a) ozone (O₃), (b) water vapour (H₂O) and (c) residual vertical velocity ($\overline{w}^*$) deseasonalised anomalies (%) for nPJO-type and PJO-type SSWs (each of which with n = 11 events) from EMAC for the time period 1980–2013. The anomalies are expressed as percentages, with the exception of the residual vertical velocity ($\overline{w}^*$) anomalies which are given in units of m s⁻¹ (zero contour represented by purple solid line). Statistical significance at the 95 % level is indicated by stippling. The World Meteorological Organization (WMO) defined thermal tropopause is displayed for reference in each panel (blue solid line).
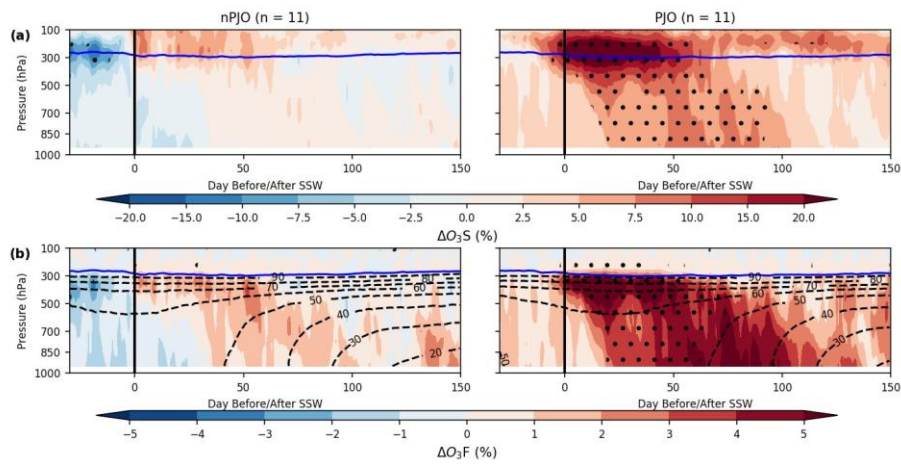
Figure 5: As Fig. 4 but for (a) ozone of stratospheric origin (O₃S) and (b) the fraction of ozone of stratospheric origin (O₃F = O₃S/O₃ x 100) deseasonalised anomalies (%) evolution for nPJO-type SSWs (n = 11) and PJO-type SSWs (1980-2013) from EMAC for the time period 1980–2013. The EMAC climatological O₃F (1980-2013) is overlaid (dashed contours) for reference in (b). Note that this seasonally evolving field is offset between nPJO and PJO cases since the mean SSW onset date differs between each event category (nPJO: 11th February and PJO: 17th January).
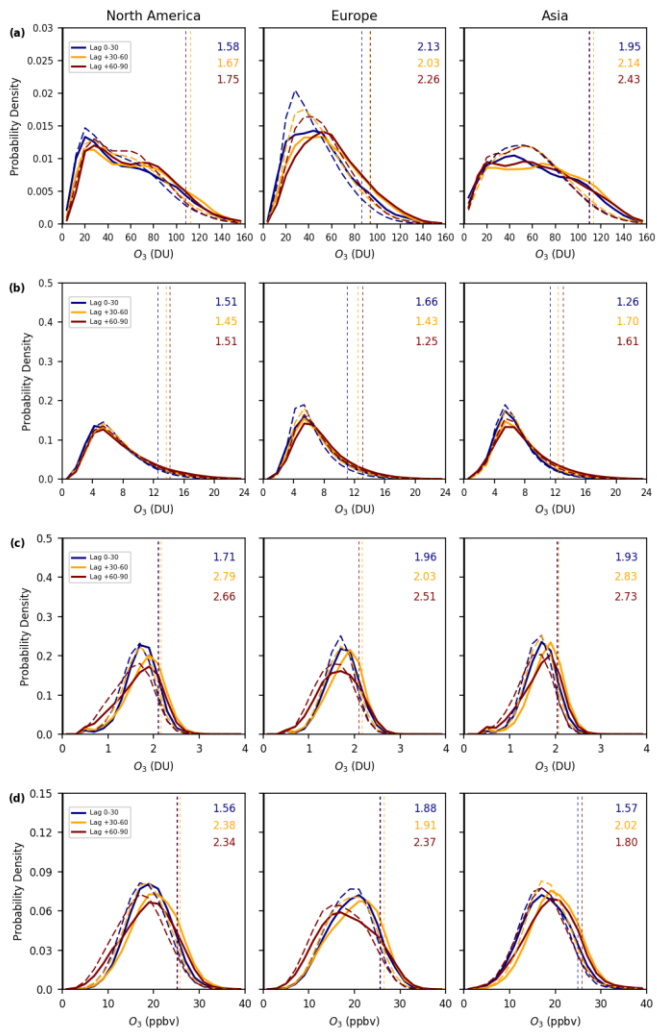
Figure 6: Time-area averaged distributions for North America (30° N–70° N, 150° W–60° W), Europe (30° N–70° N, 30° W–30° E) and Asia (30° N–70° N, 30° E–180° E) for (a) the LMS (100–300 hPa), (b) upper troposphere (300–500 hPa), (c) the planetary boundary layer (PBL) (900–1000 hPa) subcolumn ozone of stratospheric origin (O₃S), as well as (d) simulated surface O₃S mixing ratios (ppbv) for lags 0–30 days (blue lines), 30–60 days (orange lines) and 60–90 days (red lines) following the SSW central warming date. Solid lines represent SSW composite distributions and dashed lines represent the composite generated from the EMAC climatology (1980–2013), excluding SSW events. Risk ratio (RR) values of the probability of an exceedance in the 95-percentile level of each climatological distribution (dashed vertical lines) are indicated.

1025
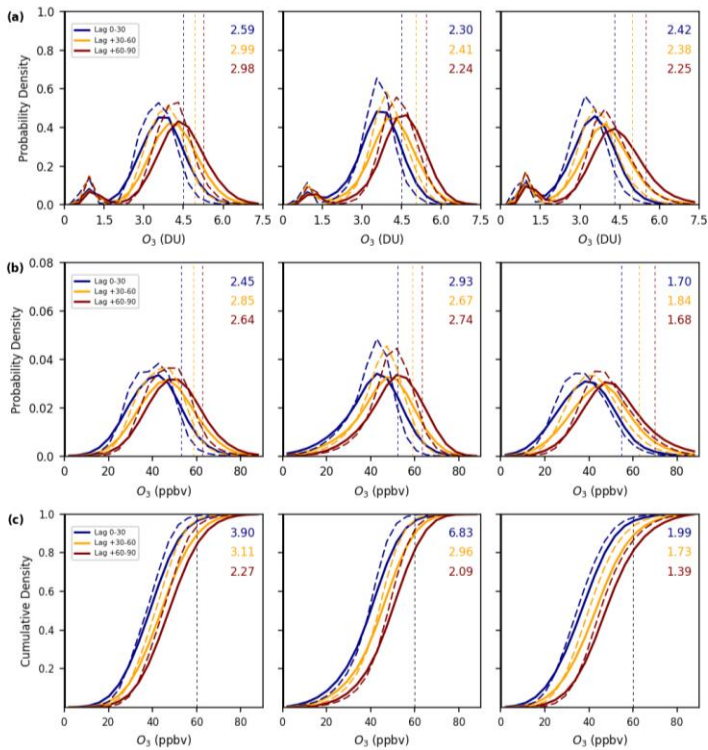
1030

Figure 7: Time-area averaged distributions for North America (30° N–70° N, 150° W–60° W), Europe (30° N–70° N, 30° W–30° E) and Asia (30° N–70° N, 30° E–180° E) for (a) the planetary boundary layer (PBL) (900-1000 hPa) subcolumn (DU) and (b) the simulated surface O_3 mixing ratio (ppbv) for lags 0–30 days (blue lines), 30–60 days (orange lines) and 60–90 days (red lines) following the SSW central warming date. The cumulative ozone distributions for the model surface level are additionally shown (c) to more clearly highlight an overall shift towards anomalously high ozone values. Solid lines represent again the SSW composited distributions and dashed lines represent the corresponding 'pseudo' climatological distributions generated from the EMAC climatology for the ozone of stratospheric origin (O_3S) component (1980–2013), excluding SSW events. Risk ratio (RR) values of the probability of an exceedance in the 95-percentile level of each climatological distribution (dashed vertical lines) are indicated, with the exception of (c) where the values represent a RR increase in the likelihood of an exceedance in the 60 ppbv threshold (a typical surface air quality standard).

1045
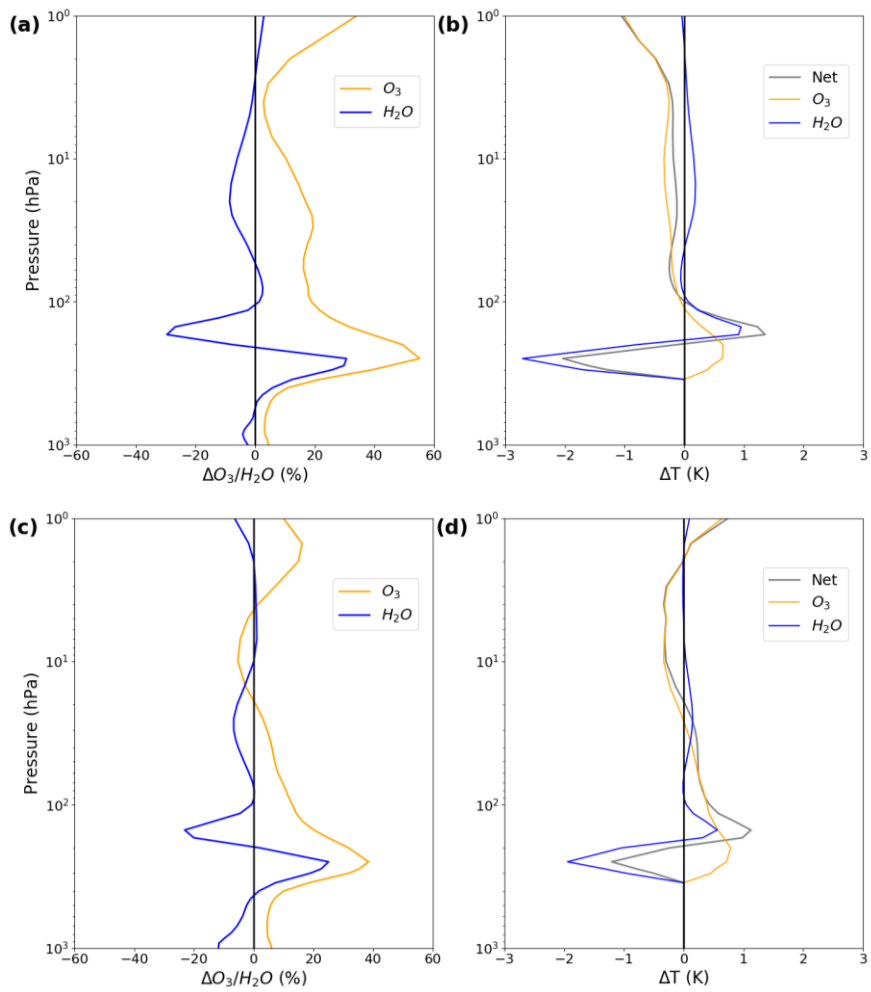
Figure 8: Polar-cap averaged (60–90° N) (a) mean perturbation to the vertical profile in ozone and water vapour (%) and (b) the resultant radiatively-driven stratospheric temperature change averaged 5 to 15 days after a PJO-type SSW (composite of 11 events over the period 1980–2013). The equivalent is shown below (c) and (d) when averaged 45 to 55 days after the mean event onset date. The grey solid line represents the net temperature change due to these composition anomalies. The FDH temperature changes are only computed at heights above the tropopause (set as 300 hPa for these calculations).

1085
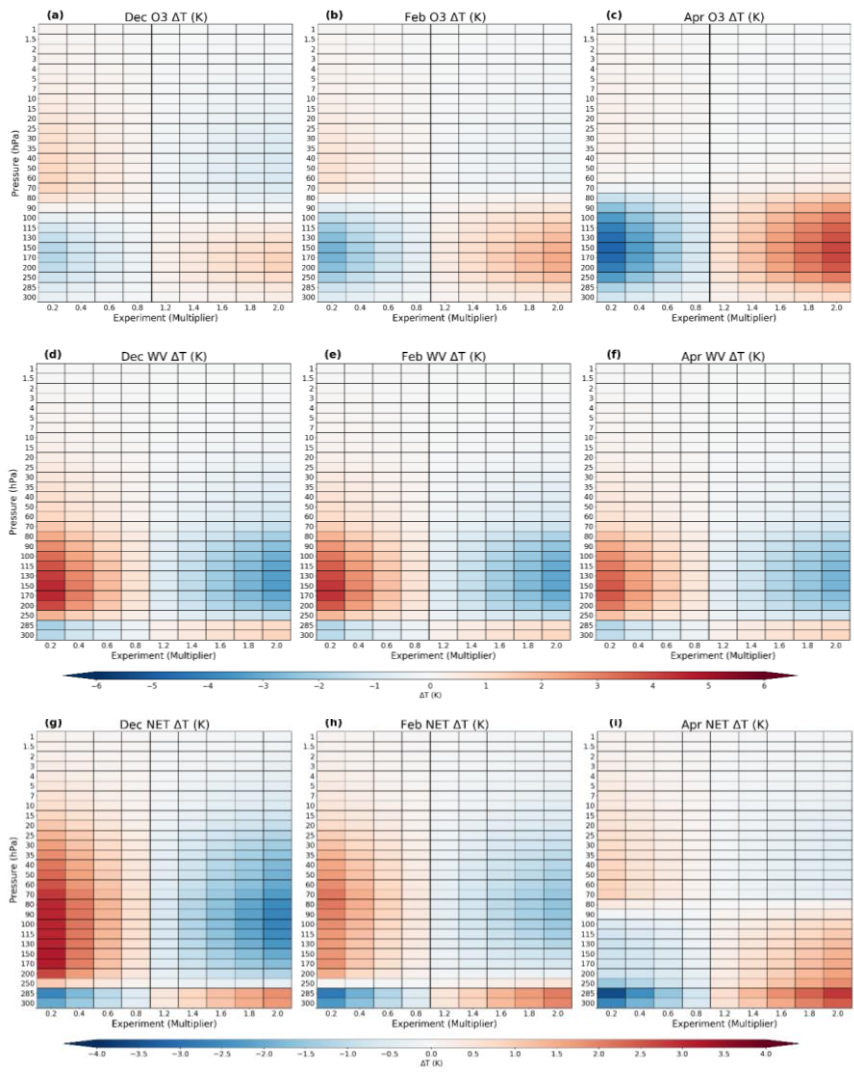
Figure 9: The idealised change in stratospheric temperature due to deviations in lower stratospheric (~70–150 hPa) ozone and/or water vapour, with respect to (a,d,g) mid-December, (b,e,h) mid-February and (c,f,i) mid-April climatology, is shown as a function of pressure (y-axis) and perturbation increment (multiplier) (x-axis). Black solid line represents a zero change in UTLS ozone abundance from climatology, with results shown for up to an 80 % reduction (multiplier of 0.2) and up to a 100 % increase (multiplier of 2.0) from left to right in each subplot.

	Alert	**Eureka**	**Ny-Ålesund**
Location	82.5° N, 62.3° W	80.0° N, 86.4° W	78.9° N, 11.9° E
Date Range	1987–2013	1998–2013	1998–2013
SSW Profiles	197	289	284
Clim Profiles	403	248	336

Table 1: The geographic latitude and longitude coordinates of the ozone-sonde sites included in this study and date range, together with the number of profiles used in calculating station mean ozone vertical profiles (100–1000 hPa) during all SSW events (0 to +70 days around an SSW central warming date) and for a station climatology (Clim) during the polar stratospheric dynamically active season. Note that the number of Clim profiles included represents all soundings from December to April inclusive, excluding all SSW profiles and those in the preceding 20 days of an event onset. The locations and mean profiles are shown in Fig. 1. All ozone-sonde profiles were convolved (averaged within ±20 hPa of the EMAC pressure levels) to reduce profile noise.